,,

People's Democratic Republic of Algeria
Ministry of Higher Education and Scientific Research

University M'Hamed BOUGARA – Boumerdes

Institute of Electrical and Electronic Engineering

Department of Electronics

Final Year Project Report Presented in Partial Fulfilment of the Requirements for the Degree of

MASTER

In **Electronics**

Option: **Computer Engineering**

Title:

Tractography of White Matter Fibers in Presence of Astrocytoma

Presented by:

- **BENOUADAH Sara**
- **ESSAHELI Mohamed Abderaouf**

Supervisor:

Dr. CHERIFI Dalila

Registration Number:...../2018

Dedication

In the beloved memory of my Grand Father who valued education above all.

To my parents, Ibrahim and Fatema, for their unconditional love, inexhaustible affection, wholehearted support and care.

To my twin sisters Madjida and Khawla for their double encouragements, teachings, and helping me develop a double-layered thick-skin.

To my younger sister Narimène, for her silly jokes, believing in me and for understanding my words and silences.

To my great families ESSAHELI and ECHIBANI.

To my friends who stood by my side all this time, for their compassion, motivation and for giving me a bit of breathing space.

To my partner Sara BENOUADAH with whom I shared this enriching journey, and who always managed to see the good things amid the chaos.

To all those who have lost a beloved one, and for all those who still fight in the battle of cancer.

To everyone who made this work possible.

I dedicate this humble work to You.

Mohamed Abderaouf

I dedicate this modest work,

To my parents Mustapha and Amel who have always supported me through their efforts, their time, their health, their continuous encouragement and support and their prayers,

to my sister Selma, who provided great support throughout the project development and who was a role model to follow, my sister Saoussen as well as my brother Mohammed Islam to whom I wish a future full of joy, happiness and success,

to my two great families BENOUADAH and MERZOUGUI,

to my friends and fellow students with whom I shared my last five years,

to my partner ESSAHELI Abdraouf whom I could always count on and who never stopped motivating me towards the best,

to all those who, by a word, gave me the strength to continue,

I dedicate this work to you and I wish you a life full of health and happiness.

Sara

Aknowledgements

First and foremost, we would like to praise Allah Almighty, for giving us the strength, knowledge and opportunity to undertake this work. Without his blessings, this piece of work would not have seen the light of day.

We would like to express our deepest gratitude to our supervisor Dr. CHERIFI Dalila , for expertly guiding all aspects of this humble work with unparalleled enthusiasm, positive energy and confidence. For all her invaluable technical and moral support, encouragements and inspiration through every step in the accomplishment of this final year project. Without her guidance and assistance, this work would not have been possible.

Forever shall we be greatly indebted to you.

Additional debts are owed to Dr. DERICHE Rachid , research director at INRIA in the Sophia Antipolis-Méditérannée Research Center, and GERARD Gabriel, researcher at Sherbrooke Connectivity Imaging Lab (SCIL), University of Sherbrooke-Canada, for their priceless suggestions and for sharing their professional remarks on our work.

We also have great pleasure to express our most sincere thanks to the entire staff of Hospital CHAHIDS MAHMDOUDI – Tizi Ouzou, starting from Dr. MAHMOUDI Said, the head of the hospital, who gave us the opportunity to work with doctors of Radiology Service. Special thanks go to Dr. KECHIH Farid, Dr. SAOUDI Massinissa and Dr.REKIK Djallel for verification and validation of our results. Mr. AIT OUAKLI Amazigh for his cooperation and help.

And we thank everyone who contributed directly or indirectly to the realization of this project.

We extend our sincere gratitude for you all.

Abstract

Diffusion Magnetic Resonance Imaging (dMRI), a technique that maps the axonal microstructure of the brain, is often used nowadays to investigate white matter alterations. Clinicians have gained useful insights from these studies for surgical planning and demonstrating subtle abnormalities in a variety of diseases.

Our work aims to identify the effects of astrocytoma, a type of tumor that affects the brain, on white matter (WM) tracts. For this purpose, three patients with different grades of astrocytomas, acquired by the UK Data Archive, are used. Constrained Spherical Deconvolution (CSD)-based deterministic tractography is applied on these datasets in order to assess the tumor-induced alterations on WM tracts. Three types of these alterations were observed: displacement of fibers around the tumor, destruction of the intralesional fibers, and destruction with displacement of the fibers within the tumoral region. A comparison is also performed between the results obtained using different reconstruction methods: Diffusion Tensor Imaging (DTI) and CSD. Although both methods confirm the existence of the tumor and its associated alterations, CSD-based tractography is most appropriate to use when dealing with tasks sensitive to intravoxel fiber connections such as the planning of a surgical procedure. Finally, a comparison between the left and right hemispheres reveals that the number of streamlines can be used to predict the existence of a tumor. The results were validated by a group of doctors and researchers in the field.

The main contributions of this work reside in determining a pattern to the effects of astrocytomas on WM tracts. While monitoring the field, we found that, among the researches investigating brain pathologies, none were particularly focused on this type of tumor. In addition, the use of CSD-based deterministic tractography while investigating brain pathologies is new in the literature, where most published articles use DTI as the only local reconstruction technique. Another contribution of this work is the comparison between the left and right hemispheres of both normal and brain tumor patients.

Keywords: dMRI, WM, astrocytoma, tumor, CSD, DTI, tractography.

Contents

List of Figures

List of Tables

List of abbreviations

ADC	Apparent Diffusion Component
AF	Arcuate Fasciculus
CC	Corpus Callosum
CSD	Constrained Spherical Deconvolution
CSF	Cerebrospinal Fluid
CST	Corticospinal Tract
DIPY	Diffusion Imaging in Python
dMRI	diffusion Magnetic Resonance Imaging
dODF	diffusion Orientation Distribution Function
DSI	Diffusion Spectrum Imaging
DTI	Diffusion Tensor Imaging
FA	Fractional Anisotropy
FACT	Fiber Assignment by Continuous Tracking
FOD	Fiber Orientation Density
fODF	fiber Orientation Density Function
FRT	Funk-Radon transform
GM	Gray Matter
HARDI	High Angular Resolution Diffusion Imaging
MD	Mean Diffusivity
MI-Brain	Medical Imaging Brain
MRI	Magnetic Resonance Imaging
NMR	Nuclear Magnetic Resonance
PDF	Probability Density Function
QBI	Q-ball Imaging
RGB	Red Green Blue
RK4	Runge-Kutta 4
ROI	Region Of Interest
SD	Spherical Deconvolution
SD	Standard Deviation
SH	Spherical Harmonics
SLF	Superior Longitudinal Fasciculus
TEND	Tensor Deflection
WHO	World Health Organization
WM	White Matter
uODF	uncertainty Orientation Distribution Function

General Introduction

The human brain is a remarkably complex organ mainly constituted of grey matter areas internally connected through bundles of myelinated axons known as the white matter (WM). The integrity of WM wirings have been proved to influence vision, sensorimotor processing, episodic memory and language. Therefore, mapping its micro-structure at fiber resolution helps gain insight into the brain connectivity in an attempt to study its function and development. This goes unfortunately beyond conventional magnetic resonance imaging (MRI).

Diffusion magnetic resonance imaging (dMRI) is a recently developed technique based on MRI. Its ability to noninvasively quantify the diffusion rate of water molecules makes it a powerful tool to accurately probe the micro-architecture of the underlying white matter structure.

Though it is relatively new technique, dMRI field counts several models and acquisition schemes including Diffusion Tensor Imaging (DTI) and High Angular Resolution diffusion Imaging (HARDI) techniques. These models exploit fiber-orientation related information to 3D-reconstruct fiber trajectories by means of deterministic or probabilistic tractography. Thereby, tractography assists neurosurgeons for surgical planning since it allows to locate, identify and study pathological changes in WM.

Among the numerous brain pathologies affecting WM fiber pathways, astrocytomas are one of the most prevalent type of brain tumors. These neoplasms induce alterations in the WM leading to behavioral and functional impairment.

This work focuses primarily on investigating the effect of astrocytoma on WM tracks by means of implementation of DTI and Constrained Spherical Deconvolution (CSD) -based deterministic tractography algorithms. This is achieved by making as few prior assumptions about the influence of this type of brain tumors on the WM track as possible, conducting therefore a data-driven approach instead. To carry out this project, the report has been divided into three chapters, briefly described bellow :

Chapter I introducing the concepts and physical principles behind diffusion MRI and state of the art techniques used to quantify this diffusion. Generalities about astrocytomas are also provided alongside few assumptions about how these brain tumors would modify WM structure.

Chapter II presents an overview about different existing reconstruction methods and tractography algorithms. Particular attention is paid to Diffusion Tensor Imaging, Spherical Deconvolution Techniques and deterministic Tractography which are at the heart of this study. The advantages and limitations of different approaches are also addressed to highlight where each method should be used.

The theoretical knowledge gained throughout the previously stated chapters, is applied in Chapter III. In this latter an examination of clinical cases is conducted through the implementation of the previously introduced methods on a platform for the analysis of Diffusion Imaging in Python (Dipy). The study qualitatively and quantitatively assesses the results of reconstruction and tractography to determine the effect of tumors on its surrounding WM tracts.

Chapter 1

Diffusion MRI

1.1 Introduction

Since the 1980s, diffusion magnetic resonance imaging (dMRI) has been used to track the diffusion of water molecules in the human brain *in vivo* and non-invasively. This technique allows one to map the microstructure and organization of brain pathways. Due to these unique properties, dMRI has gained great significance in the clinical field, for instance, using the measurements obtained in pre-surgical planning, the identification of disease biomarkers, as well as the investigation of tumors effect on white matter tissue integrity which will be the main focus of our work. In this chapter, we will introduce the concepts related to diffusion MRI, and the state-of-the-art techniques used to measure this diffusion. We will also take an interest to the clinical applications of this technique.

1.2 Concepts of molecular diffusion

Macroscopically, molecular diffusion is defined as the process by which molecules are transported from a high to a low concentration region, which decreases the concentration gradient. In 1855, Adolf Fick was the first to give a mathematical description of this phenomenon (Fick, 1995). Fick's first law states:

$$J = -D\nabla C \tag{1.1}$$

where J is the net particle flux (unit: mol/ms), C is the particle concentration (unit: mol/m3), and D is the diffusion coefficient (unit: m^2/s).

If we consider a closed system, the number of particles is preserved. This operation is described by the continuity equation, which states that the divergence of the flux is equal to the negative rate of the change in concentration:

$$\frac{\partial C}{\partial t} = -\nabla J \tag{1.2}$$

By combining equation 1.2 with Fick's first law and considering the coefficient of diffusion, D, as a constant, we obtain the following diffusion equation:

$$\frac{\partial C}{\partial t} = D\nabla^2 C \tag{1.3}$$

In the case of a boundless model with spatially uniform diffusion, the solution of the diffusion equation is given by equation 1.4. By setting the initial condition: $C(p_t, 0) = \delta(p_t - p_0)$, where p_t is the position of the molecule at time t, and p_0 the initial position at t = 0. We have:

$$C(p_t, t) = \left(\frac{1}{\sqrt{4\pi Dt}}\right)^3 e^{-\frac{(p_t - p_0)^2}{4Dt}} \tag{1.4}$$

This equation shows that the evolution of the concentration over time follows a Gaussian distribution (Clarisse, 2008); and that the particle concentration at position pt at time t depends on the diffusion coefficient D.

1.2.1 Brownian motion

Another approach is to measure the diffusion coefficient by monitoring the process of diffusion itself. Indeed, while in equilibrium conditions the macroscopic description does not suggest diffusion, the molecules still present a random movement caused by thermal energy. This phenomenon, illustrated in Figure 1.1, is called Brownian motion, named after the botanist Robert Brown, who was the first to write a report on this random movement of particles (Brown, 1828).

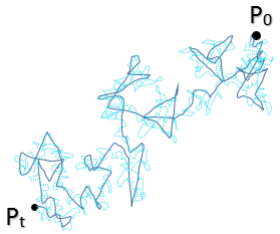

Figure 1.1: Simulation of the Brownian motion of a particle in two dimensions. The molecule is at point pt at time t and initially at point p0.

In 1905, Einstein (Einstein, 1956) used a probabilistic model to describe this movement; he introduced the notion of "propagator", which allowed to give the probability of a particle

moving a certain distance during a given time interval. In a free medium, during a given time interval, molecular displacements obey a Gaussian distribution, described as follows:

$$P(p_t, t) = \left(\frac{1}{\sqrt{4\pi Dt}}\right)^3 e^{-\frac{(p_t - p_0)^2}{4Dt}} \tag{1.5}$$

The width of this Gaussian function is determined by the diffusion coefficient (Johansen-Berg & Behrens, 2013) as illustrated in Figure 1.2:

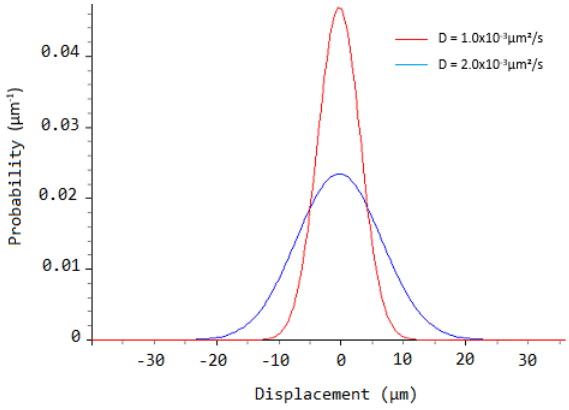

Figure 1.2: Gaussian distribution of molecular displacement for two different values of the diffusion coefficient with a diffusion time of 40ms.

Larger diffusion coefficients (as illustrated in Figure 1.2 (blue)) lead to more spread out probabilities of displacement suggesting increased diffusion.
Einstein then proved that the mean squared displacement traveled by a molecule during a time interval, t, is proportional to the diffusion coefficient, D, of the considered medium:

$$\left\langle (p_t - p_0)^2 \right\rangle = 6Dt \tag{1.6}$$

The diffusion coefficient is a scalar that depends solely on the size of the molecules, the temperature and the viscosity of the medium (Le Bihan, 2003). From equation 1.6, we can directly deduce the diffusion coefficient by measuring the displacement of the molecules.

1.2.2 Isotropic vs. Anisotropic diffusion

The distance that a molecule diffuses in one direction in space may or may not be the same as in some other direction. Clearly, in a pure liquid where there are no hindrances to diffusion or in a sample where the barriers are not coherently oriented, diffusion is the same in all directions and is termed *isotropic* diffusion. However, if diffusion depends on a certain direction, like in a sample with highly oriented barriers, it is termed *anisotropic* diffusion. This is well illustrated in Figure 1.3.

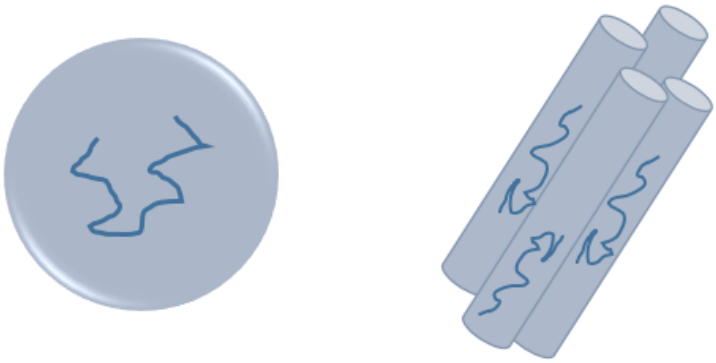

(a) Diffusion in isotropic sample (b) Diffusion in anisotropic sample

Figure 1.3: An illustration depicting diffusion in two different types of samples, one (a) which has similar molecular displacements in all directions (isotropic diffusion) and the other (b) which has greater diffusion along one direction over another (anisotropic diffusion).

In this way, structural subtypes can be identified simply on the basis of their diffusion characteristics and the anisotropy is directly related to the geometry of the fibers (Beaulieu, 2002).

1.2.3 Diffusion tensor model

In the case of anisotropic diffusion, the scalar diffusion coefficient is no longer sufficient to describe the phenomenon of diffusion. Another concept must be used: *the diffusion tensor* $\boldsymbol{D}$. The exploitation of this tensor allows the determination of the principle direction of diffusion. The diffusion tensor (Basser & Pierpaoli, 1998) is a 2nd order tensor and the components are given by a 3 x 3 symmetric, positive definite matrix.

$$D = \begin{bmatrix} D_{xx} & D_{xy} & D_{xz} \\ D_{yx} & D_{yy} & D_{yz} \\ D_{zx} & D_{zy} & D_{zz} \end{bmatrix} \tag{1.7}$$

with Dyx = Dxy , Dxz = Dzx , Dyz = Dzy.
We will discuss this in more detail in the next chapter.

1.3 Diffusion in the human brain

In the brain, biological tissues are very heterogeneous. The underlying cellular microstructure of these tissues influences the overall mobility of the diffusing molecules by providing numerous barriers and by creating various individual compartments (e.g. intracellular, extracellular, neurons, glial cells, axons) within the tissue. The interactions

between water molecules and these barriers greatly reduce the diffusion distance compared to the case of free diffusion, and in general the diffusion displacement can no longer follow a Gaussian distribution. In this case, we speak of restricted (anisotropic) diffusion (Figure 1.4). It should be noted that only over long diffusion times will the effects of the barriers become apparent (Beaulieu, 2002).

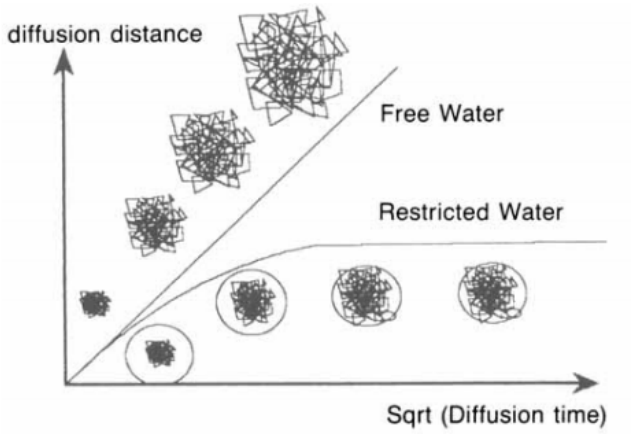

Figure 1.4: The mean distance traveled by water molecules in the case of "free" diffusion, and in the case of "restricted" diffusion. Figure from (Le Bihan *et al.*, 1991)

The brain presents three structures that modulate the diffusion: cerebrospinal fluid (CSF), gray matter (GM) and white matter (WM) (Figure 1.5).

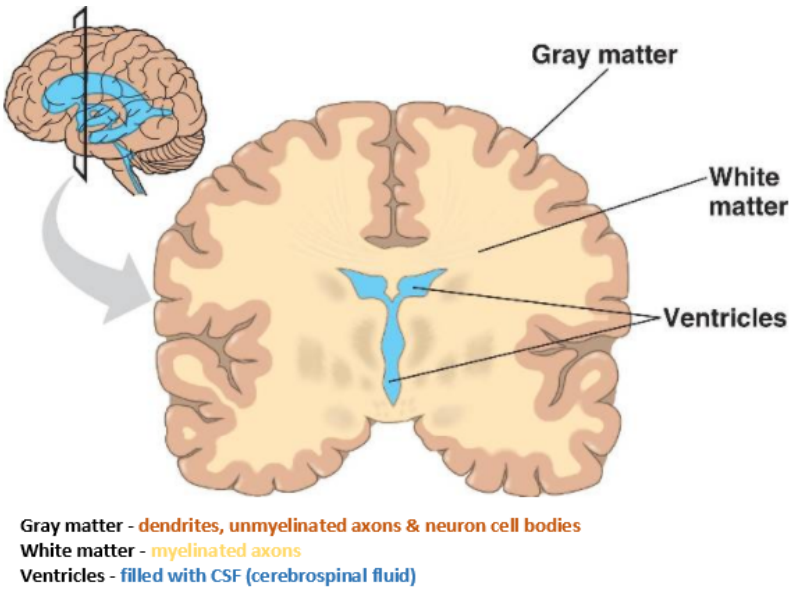

Figure 1.5: Human brain coronal slice showing the three major tissue types.

The diffusion of water molecules in CSF can be assimilated to the diffusion in homogeneous medium of low viscosity. The diffusion is therefore important and identical in all directions

of space (isotropic diffusion). GM and WM, which are more viscous, have lower diffusion coefficients. However, the underlying structure of each of these tissues gives rise to very different diffusion properties. The GM is the tissue containing cell bodies, which makes the diffusion quasi-isotropic. WM, on the other hand, is organized in very large bundles of axons. This anisotropic structure greatly affects diffusion, making it faster in the direction of the fibers (axons) and less significant across them (Tensaouti, 2010). This is illustrated in Figure 1.6.

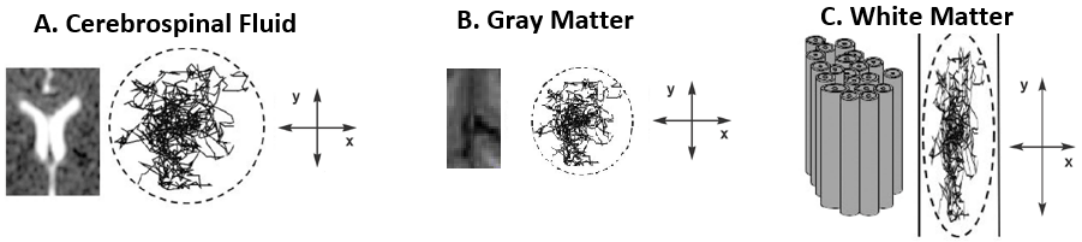

Figure 1.6: An illustration showing the diffusion characteristics in the major tissue types of the brain. (A) in CSF, (B) in GM, and (C) in WM.

In our work, we are mainly interested in diffusion at the WM level and have focused our efforts on the study of fiber orientation, using the information provided by the diffusion MRI. This information is then processed and interpreted using mathematical tools that we will see later.

1.4 Diffusion Measurement: Pulsed Gradient Spin Echo

The aim of diffusion MRI is to obtain images by exploring the micro-movements of water molecules inside voxels. This technique makes it possible to quantify the anisotropy of diffusion, in order to reconstruct the global orientation of the nerve fibers inside WM.
Water is an abundant source of hydrogen nuclei (protons), which are detectable by an MRI scanner. All hydrogen nuclei possess a quantum mechanical property known as spin, which determines their intrinsic magnetic moment; each proton can be considered loosely as a tiny bar magnet.
To measure diffusion, the Stejskal–Tanner imaging sequence is used (Stejskal & Tanner, 1965). This sequence uses two strong gradient pulses, symmetrically positioned around a 180° refocusing pulse, allowing for controlled diffusion weighting (Figure 1.7). The first gradient pulse induces a phase shift for all spins; the second gradient pulse will invert this phase shift, thus canceling the phase shift for static spins. Spins having completed a change of location due to Brownian motion during the time period, $\triangle$, will experience different phase shifts by the two gradient pulses, which means they are not completely refocused

and consequently will result in a signal loss.

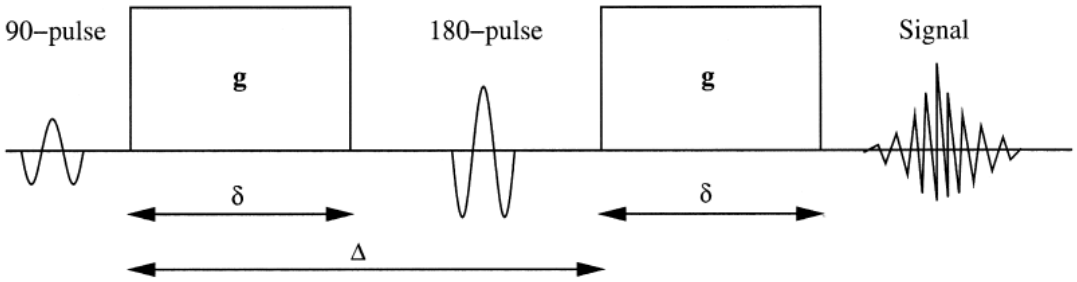

Figure 1.7: The Stejskal-Tanner imaging sequence. Figure from (Westin *et al.*, 2002)

To eliminate the dependence of spin density, T1 and T2, we must take at least two measurements of diffusion-weighted images that are differently sensitized to diffusion but remain identical in all other aspects. By using, for instance, a measurement without diffusion weighting and one with diffusion weighting. Diffusion can be calculated using the following equation (Stejskal & Tanner, 1965):

$$S = S_0 e^{-bD} \tag{1.8}$$

where b is the diffusion weighting factor, introduced and defined by (Le Bihan *et al.*, 1986),

$$b = \gamma^2 \delta^2 \left(\Delta - \frac{\delta}{3} \right) |g|^2 \tag{1.9}$$

where ɣ is the proton gyromagnetic ratio, |g| is the strength of the diffusion sensitizing gradient pulses, δ is the duration of the diffusion gradient pulses, and $\triangle$ is the time between diffusion gradient RF pulses (Figure 1.7). This emphasizes the fact that the diffusion tensor values, D, also known as 'apparent diffusion components' (or ADC values), generated from this procedure depend on the experimental conditions such as the direction of the sensitizing gradient and other sequence parameters (δ and $\triangle$).

1.5 Clinical application

Reconstructing and visualizing the microstructure of WM is one of the greatest achievements of dMRI. However, this can be more rewarding when applied on patients with brain pathologies. In brain tumor patients, pre-operative surgical planning and assessment of the surrounding WM tracts is a very important step to allow complete resection of tumor, while at the same time avoiding recurrence and loss of vital brain functions. Conventional MRI techniques can accurately identify brain tumors but do not provide exhaustive infor-

mation about the integrity of the surrounding white matter (Essayed *et al.*, 2017). dMRI and specifically tractography technique is currently the only available tool which displays the WM tracts disruption by fractional anisotropy changes in patients with brain tumors. A number of brain pathologies affect WM fiber pathways, one example is astrocytoma.

Astrocytomas are tumors that grow from a type of cell in the brain called an astrocyte. They are the most common type of a group of brain tumors called gliomas and account for about one third of all brain tumors. There are various types of astrocytomas, each of which affect both adults and children (thebraintumourcharity.org). Brain tumors are graded by the World Health Organization (WHO) from 1 - 4, according to how they behave i.e. how fast they grow and how likely they are to spread within the brain. Astrocytomas can be any grade, from 1 - 4.

Depending on the grade of the tumor, the effects astrocyomas have on WM fiber pathways may vary. In fact, while high-grade aggressive lesions are thought to significantly alter morphology and impair functionality of infiltrated WM, less aggressive tumors may simply displace the surrounding brain structures. The surgical strategy, which mainly aims at finding the best compromise between amount of tissue removed and degree of preservation of brain functionality, is susceptible to the resulting metamorphosis. This study aims to investigate the different tumor-induced alterations of WM architecture in order to accurately localize and assess the damaged WM tracts for preoperative surgical planning and intra-operative decision-making.

1.6 Summary

The diffusion of water is produced by the random movement of water molecules due to thermal energy. Diffusion MRI is an imaging modality that allows to observe the diffusion of water molecules at the microscopic level in the brain. It is a technique that found great importance because of its ability to give information of the brain microstructure in vivo and non-invasively. Due to these unique qualities, dMRI found great importance in the neurosurgical field, specifically in the pre-surgical planning and the investigation of different brain pathologies. The acquisition of the raw diffusion images is based on the principle of nuclear magnetic resonance (NMR) combined with a diffusion gradient echo sequence. In the next chapter, we will introduce the step that follows the acquisition of dMRI data, which entails the estimation of the local fiber orientations and the 3 dimensional reconstruction of fiber trajectories.

Chapter 2

Reconstruction Methods and Tractography

2.1 Introduction

A large amount of information can be extracted from the diffusion MRI data. This information is processed to provide us with the fiber pathways in WM. This essential step towards connectivity maps of the brain is called tractography. Before reconstructing the fiber trajectories, however, the voxel-wise fiber orientations need to be estimated. Thus, methods such as DTI and HARDI based approaches were developed. Several tractography methods exist that reconstruct the trajectories of WM fibers from the previously estimated orientations. These trajectories are often represented by threadlike fascicles more or less thick. This form of representation is purely visual. The diffusion measurement only indirectly reflects the structure of WM, there are several orders of magnitude between the resolution of diffusion MRI acquisitions and the diameter of the axons. The reconstructed fibers correspond rather to bundles of axons of the same order of magnitude as a voxel that-is-to-say of more than one millimeter in diameter. Therefore, the tractography is able to map only the large bundles of the WM.

This chapter is divided into two major sections, reconstruction methods and tractography. The purpose of each section is to provide the reader with an overview of the different existing reconstruction techniques and tractography algorithms, respectively.

2.2 Reconstruction Methods

Several models and techniques are used to estimate the white matter wiring, in this chapter, we will introduce the Diffusion Tensor Imaging method along with the High Angular Resolution Diffusion Imaging techniques.

2.2.1 Diffusion Tensor Imaging (DTI)

Since its introduction in early 90s, Diffusion Tensor Imaging (DTI) (Basser *et al.*, 1994a,b) has gained popularity among clinicians and researchers. This technique provides insights in the axonal microstructure of the brain through estimation of diffusion anisotropy and principal axonal direction in the white matter fibers.

2.2.1.1 Tensor Calculation

DTI exploits the assumption that the probability of diffusion in a homogeneously aligned system follows a Gaussian diffusion resulting in an elliptical shape -also known as- the diffusion ellipsoid (Basser *et al.*, 1994a,b; Pierpaoli *et al.*, 1996).
One way to reconstruct the diffusion ellipsoid is by taking measurements of the Apparent Diffusion Coefficients (ADCs) along a small number of orientations. This process requires the use of the previously mentioned diffusion Tensor, from where the denomination of this technique "*Diffusion Tensor Imaging*" (DTI).

In order to achieve a full characterization of the diffusion ellipsoid, six parameters are required; these parameters include the different lengths for the shortest, middle and longest axes needed to define the shape of the ellipsoid; and three vectors to define the orientation of the principal axes.
Since six parameters are needed to define the diffusion ellipsoid, six measurements of diffusion constants along six arbitrary axis are conducted.

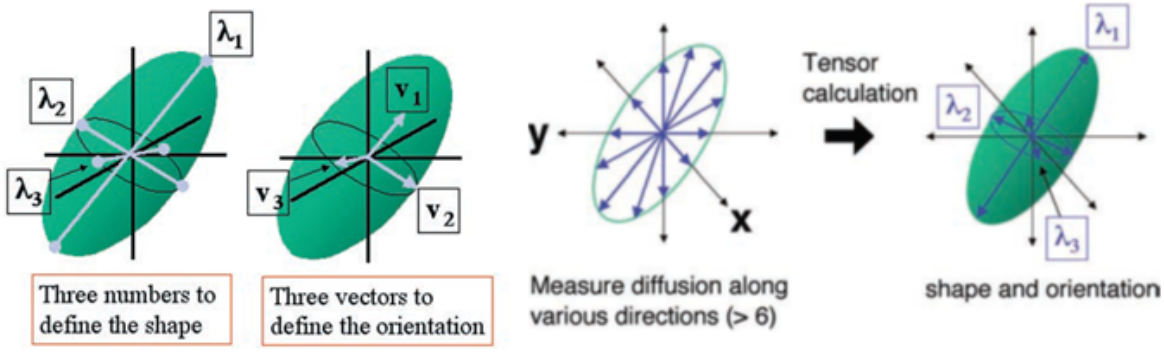

Figure 2.1: Visual representation of the diffusion ellipsoid.

The Diffusion tensor D used to keep record of these values, is a 3×3 symmetric matrix related to the six parameters via Diagonilization process. Where λ_1, λ_2 and λ_3 are the Eigen values, and v_1, v_2 , v_3 are the Eigen vectors.

$$D = \begin{bmatrix} D_{xx} & D_{xy} & D_{xz} \\ D_{yx} & D_{yy} & D_{yz} \\ D_{zx} & D_{zy} & D_{zz} \end{bmatrix} \xrightarrow{Diagonalization} \lambda_1, \lambda_2, \lambda_3, v_1, v_2, v_3 \tag{2.1}$$

Whereas the gradient direction can be represented by a three element column vector g.

$$g = \begin{bmatrix} g_x \\ g_y \\ g_z \end{bmatrix} \tag{2.2}$$

In order to measure six diffusion constants, a minimum of seven MR images is required (Basser & Pierpaoli, 1998) one without any diffusion sensitizing gradients applied and at least six diffusion-weighted images with gradients applied in non-collinear directions. Mathematically, only six non-collinear diffusion-weighted directions are necessary to reconstruct the diffusion tensor; however, in practice more images should be acquired to improve the accuracy of tensor estimation (Jones, 2004).
To evaluate tensor D for a given direction, the following expression is used:

$$g^T Dg = g_x^2 D_{xx} + g_y^2 D_{yy} + g_z^2 D_{zz} + 2g_x g_y D_{xy} + 2g_x g_z D_{xz} + 2g_y g_z g_{yz} \tag{2.3}$$

where g^T is the transpose of g.
The result of this expression is a scalar number representing the value of the tensor model along a given direction. By combining this with the Stejskal-Tanner equation 1.8 we obtain the following expression:

$$S = S_0 e^{-bg^T Dg} \tag{2.4}$$

This can be rewritten as:

$$g^T Dg = \frac{-ln(\frac{S}{S_0})}{b} \tag{2.5}$$

Expending the left side by plugging equation 2.3 in 2.5, results into:

$$g_x^2 D_{xx} + g_y^2 D_{yy} + g_z^2 D_{zz} + 2g_x g_y D_{xy} + 2g_x g_z D_{xz} + 2g_y g_z g_{yz} = \frac{-ln(\frac{S}{S_0})}{b} \tag{2.6}$$

In equation 2.6, S, b and g are all known. Whereas the six unknown parameters characterizing the Diffusion Tensor Model would require at least six similar equations denoting the measurement of diffusion along six arbitrary axes, in addition to S_0 denoting the b_0 value signal used to normalize measurements. With this in hand the resulting set of equations would be:

$$g_i^T D g_i = \frac{-ln(\frac{S_i}{S_0})}{b_i},\ i \in 1, ..., M \tag{2.7}$$

where M is the number of gradients applied. This leads to:

$$-b_i \begin{pmatrix} g_{1,x}^2 & g_{1,y}^2 & g_{1,z}^2 & 2g_{1,x}^2 g_{1,y}^2 & 2g_{1,x}^2 g_{1,z}^2 & 2g_{1,y}^2 g_{1,z}^2 \\ ... & ... & ... & ... & ... & ... \\ g_{M,x}^2 & g_{M,y}^2 & g_{M,z}^2 & g_{M,x}^2 g_{M,y}^2 & g_{M,x}^2 g_{M,z}^2 & g_{M,y}^2 g_{M,z}^2 \end{pmatrix} \begin{pmatrix} D_{xx} \\ D_{yy} \\ D_{zz} \\ D_{xy} \\ D_{xz} \\ D_{yz} \end{pmatrix} = \begin{pmatrix} ln\left(\frac{S_1}{S_0}\right) \\ . \\ . \\ . \\ ln(\frac{S_M}{S_0}) \end{pmatrix} \tag{2.8}$$

Determining the six unknown values relies on solving this set of equations, for this, the Linear Least Square technique is used (Cherifi *et al.*, 2013); where the corrsponding variables of the equation $x^* = (A^T A)^{-1} A^T Y$ are:

$$x^* = \begin{pmatrix} D_{xx} \\ D_{yy} \\ D_{zz} \\ D_{xy} \\ D_{xz} \\ D_{yz} \end{pmatrix} \tag{2.9}$$

$$A = -b_i \begin{pmatrix} g_{1,x}^2 & g_{1,y}^2 & g_{1,z}^2 & 2g_{1,x}^2 g_{1,y}^2 & 2g_{1,x}^2 g_{1,z}^2 & 2g_{1,y}^2 g_{1,z}^2 \\ ... & ... & ... & ... & ... & ... \\ g_{M,x}^2 & g_{M,y}^2 & g_{M,z}^2 & g_{M,x}^2 g_{M,y}^2 & g_{M,x}^2 g_{M,z}^2 & g_{M,y}^2 g_{M,z}^2 \end{pmatrix} \tag{2.10}$$

$$Y = \begin{pmatrix} ln\left(\frac{S_1}{S_0}\right) \\ . \\ . \\ . \\ ln(\frac{S_M}{S_0}) \end{pmatrix} \tag{2.11}$$

2.2.1.2 Diffusion Tensor Measures

Once the Diffusion Tensor is obtained, several rotationally invariant quantities can be extracted such as the trace of the DT, the apparent diffusion Coefficient (ADC), or the fractional anisotropy (FA), among others (Descoteaux, 2015). These parameters deliver important information and are in function of eigenvalues and eigenvectors of the tensor.

By performing an eigenvalue decomposition on the diffusion tensor, one would be left with the eigenvalues along with their corresponding eigenvectors as shown in equation 2.12:

$$D = E\Lambda E^T = \begin{pmatrix} e_1 & e_2 & e_3 \end{pmatrix} \begin{pmatrix} \lambda_1 & 0 & 0 \\ 0 & \lambda_2 & 0 \\ 0 & 0 & \lambda_3 \end{pmatrix} \begin{pmatrix} e_1^T \\ e_2^T \\ e_3^T \end{pmatrix} \tag{2.12}$$

With eigenvalues λ_1, λ_2 and λ_3 such that$\lambda_1 \geq \lambda_2 \geq \lambda_3$, and e_1, e_2 and e_3 as their corresponding eigenvectors.
The reconstruction of white matter bundles depends on the largest eigenvalue which determines the principal direction of the diffusion tensor at a given voxel.
With the eigenvalues and eigenvectors at hand, the most important parameters can be defined as follow:

$$MD = \frac{\lambda_1 + \lambda_2 + \lambda_3}{3} \tag{2.13}$$

$$FA = \sqrt{\frac{3}{2}} \cdot \sqrt{\frac{(\lambda_1 - MD)^2 + (\lambda_2 - MD)^2 + (\lambda_3 - MD)^2}{\lambda_1^2 + \lambda_2^2 + \lambda_3^2}} \tag{2.14}$$

The mean diffusivity (MD) is simply the average of the three eigenvalues, it is a rotationally invariant measure which describes the overall shape of the tensor. Whereas the fractional anisotropy (FA) is a normalized, rotationally invariant measure of how much the eigenvalues differ. Higher FA values denote higher anisotropy and therefore reflects regions with densely packed white matter bundles oriented in the same direction.
These parameters are illustrated in Figure 2.2 along with the RGB map, which is a directionally-encoded color FA map, where the red, green, and blue colors each represents the x-, y-, and z-directions of water diffusion respectively, and the brightness of the pixels corresponds to anisotropy.

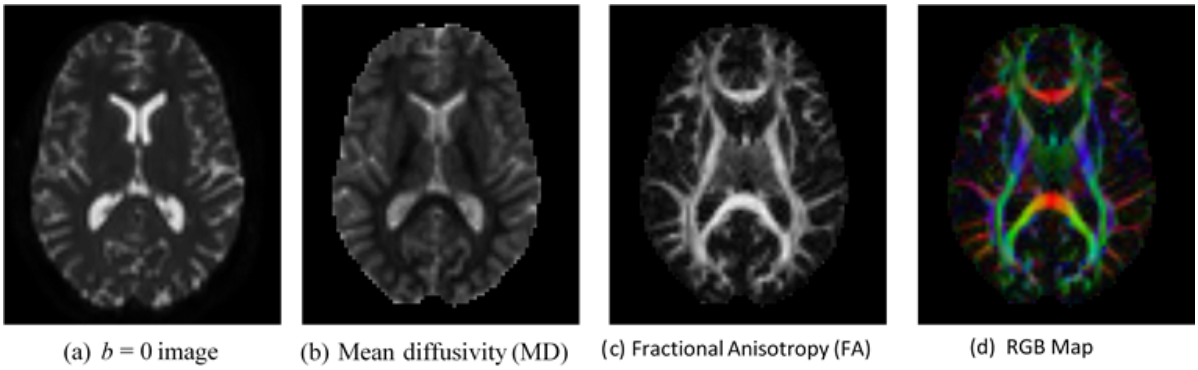

Figure 2.2: Examples of DTI scalar maps. (a) Non-diffusion weighted image b=0; (b) MD map; (c) FA map; (d) RGB map.

2.2.1.3 Diffusion Tensor Imaging Limitations

Though DTI is a powerful tool for modeling homogeneously aligned bundles, it fails to give a realistic and practical description of the white matter microstructure. This is due to the fact that specific regions of the brain containing two or even more differently oriented fiber bundles within the same voxel (crossing, diverging, or kissing fibers) lead to incorrect estimation of fiber directions and pathways (Soares *et al.*, 2013). Moreover, it has been shown that crossing fibers can be detected in over 90% of white matter voxels (Jeurissen *et al.*, 2010).

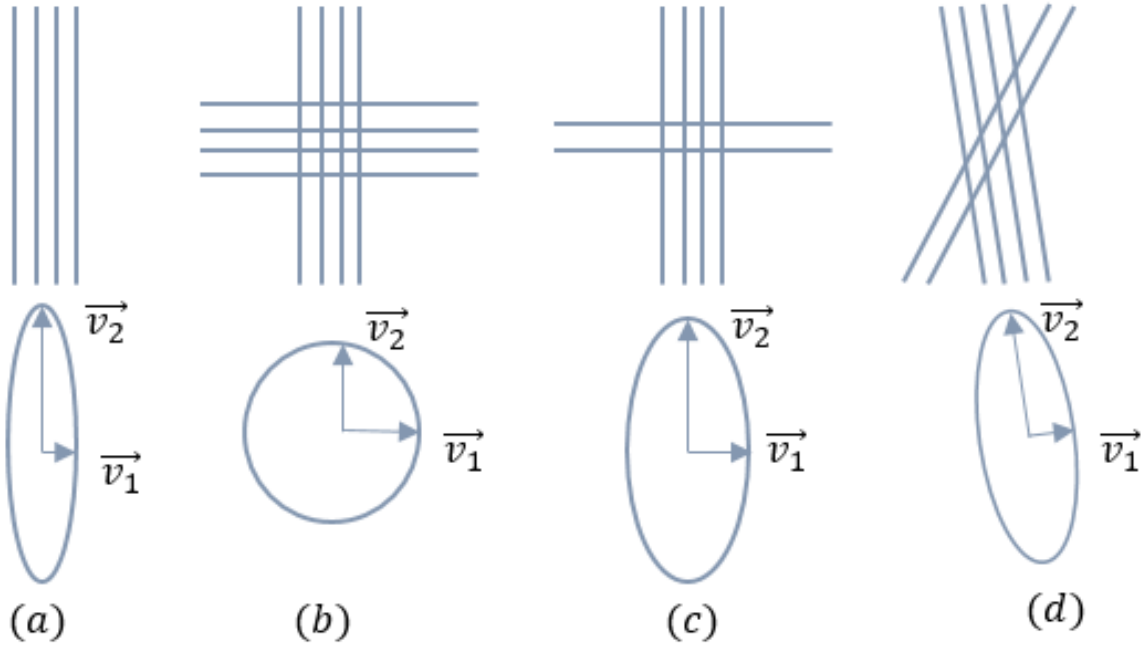

Figure 2.3: The figure represents various configurations of crossing fibers along with their corresponding 2D diffusion ellipsoids. Lines represent different fiber populations and their amount.

In order to overcome the limitations of DTI, several sophisticated models and approaches have been suggested including High Angular Resolution Diffusion Imaging which will be introduced in the next section.

2.2.2 High Angular Resolution Diffusion Imaging Techniques

In order to address the limitations of the DTI method, more sophisticated models based on High Angular Resolution Diffusion-Weighted Imaging (HARDI) were developed. HARDI refers to an acquisition technique which relies on extensive sampling along a large number of axes (i.e. High Angular Resolution) using a single b-value larger than b-values usually used for DTI.

The HARDI based methods offer a more reliable microscopic architecture of WM tissue especially in regions of fiber populations with different orientations. They aim to describe diffusion of water molecules in each voxel by estimating the probability density function (PDF) or variants of it which is capable of inferring diffusion in any kind of fiber population. There are two major sampling schemes used in HARDI (Paragios *et al.*, 2010):

1. Whole q-space 3D Cartesian grid sampling.
2. Single Shell Spherical Sampling.

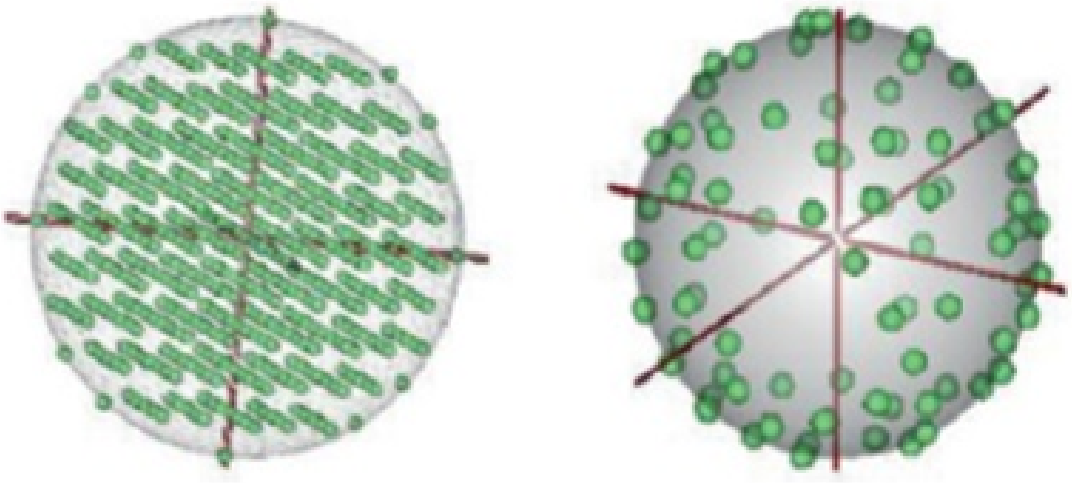

Figure 2.4: HARDI acquisition strategies: (Left) sampling over the Cartesian grid. (Right) sampling on a single spherical shell.

The first sampling scheme is mainly used for Diffusion Spectrum Imaging (DSI), it consists of estimating the diffusion PDF by sampling a large number of q-space points over a dense 3D Cartesian lattice and taking afterwards the inverse Fourier Transform. This method involves the use of very high magnetic gradients during a long acquisition.
The second sampling scheme is at the core of Q-ball Imaging (QBI) and Spherical Deconvolution (SD) techniques, it consists of estimating the Orientation Distribution function or variants of it by uniform sampling on a single spherical shell with a radius determined by the b-value used. This method involves the use of b-values smaller compared to the ones used for DSI with an acquisition time between 10 and 20 minutes.

2.2.2.1 Diffusion Spectrum Imaging

Diffusion spectrum imaging (DSI) (Figure 2.5) is a technique based on q-space imaging in three dimensions (Wedeen *et al.*, 2000). It exploits the Fourier transform relationship (Equation 2.15) between the q-space diffusion signal that we measure and the real space probability density function (PDF) that describes the diffusion process of water molecules, also called the diffusion propagator p(r,t) (Descoteaux, 2015).

$$E(q,t) = \int_{R^3} p(r,t) e^{-2\pi i q^T r} dr \tag{2.15}$$

Firstly, raw diffusion-weighted signal is acquired by sampling q-space on a 3D Cartesian grid through a large number of measurements. It is then normalized using the S_0 signal resulting in E(q,t), known as signal attenuation.
The probability density function PDF is then recovered by means of Inverse Fourier transform through the following equation:

$$p(r,t) = F^{-1}\left(E\left(q,t\right)\right) \tag{2.16}$$

With the diffusion propagator in hand, the fiber orientations are identified by means of its 2D radial projection, known as the diffusion orientation density function Ψ, through identification of its peaks.

$$\Psi(\theta,\phi) = \int_0^\infty p(r,\theta,\phi) r^2 dr St.\theta \in [0,\pi], \phi \in [0,2\pi] \tag{2.17}$$

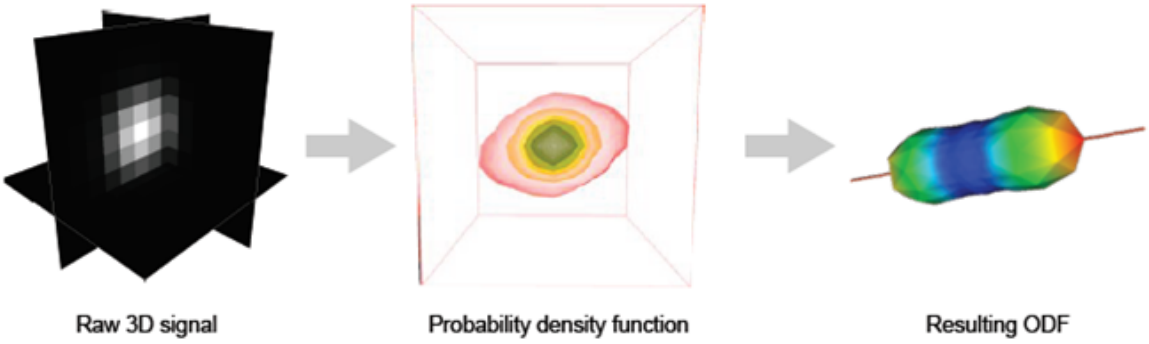

Figure 2.5: Diffusion Spectrum Imaging.

Though it is a powerful tool in resolving crossing fibers issue, DSI remains clinically infeasible due to the use of very strong magnetic gradients ($500 \leq b \leq 20000\ s/mm^2$) during long acquisition sessions (15-60 minutes).

2.2.2.2 Q-Ball Imaging

Q-ball imaging is the first method proposed to estimate the diffusion Orientation Distribution Function (dODF) (Tuch, 2004) in a significantly shorter acquisition time. It uses the Funk-Radon transform (FRT) G , to recover a smoothed version of the diffusion ODF (Equation 2.18) from a single-shell HARDI acquisition (Descoteaux & Poupon, 2012), and

is proved to be efficiently and robustly implemented using spherical harmonics (Descoteaux *et al.*, 2007; Hess *et al.*, 2006).

$$\Psi(\theta,\phi) = \int_0^\infty p(r,\theta,\phi)drSt.\theta \in [0,\pi], \phi \in [0,2\pi] \tag{2.18}$$

The Funk-Randon Transform was first introduced by Tuch (Tuch, 2004; Tuch *et al.*, 2002). It computes integrals over great circles defined over the unit sphere and is given by:

$$G[f(w)](u) = \int \delta(u^T w) f(w) dw \tag{2.19}$$

where u and w are constrained to be unit vectors and f(w) is a function on the sphere. Tuch proved that the dODF can be closely approximated using FRT of the diffusion signal in the following equation:

$$\Psi(u) = G_{q'}[S(q)](u) = 2\pi q' \int P(r,\theta,z) J_0(2\pi q' r) r dr\, d\theta dz \tag{2.20}$$

where q' is the radius of the sampling shell; P(r,θ,z) denoting the PDF in cylindrical coordinates with the z-axis taken to be along the direction of interest u, and J_0 is the 0th-order Bessel function.

The diffusion ODF recovering technique using the FRT based on the spherical harmonics formulation can be summarized in the following figure.

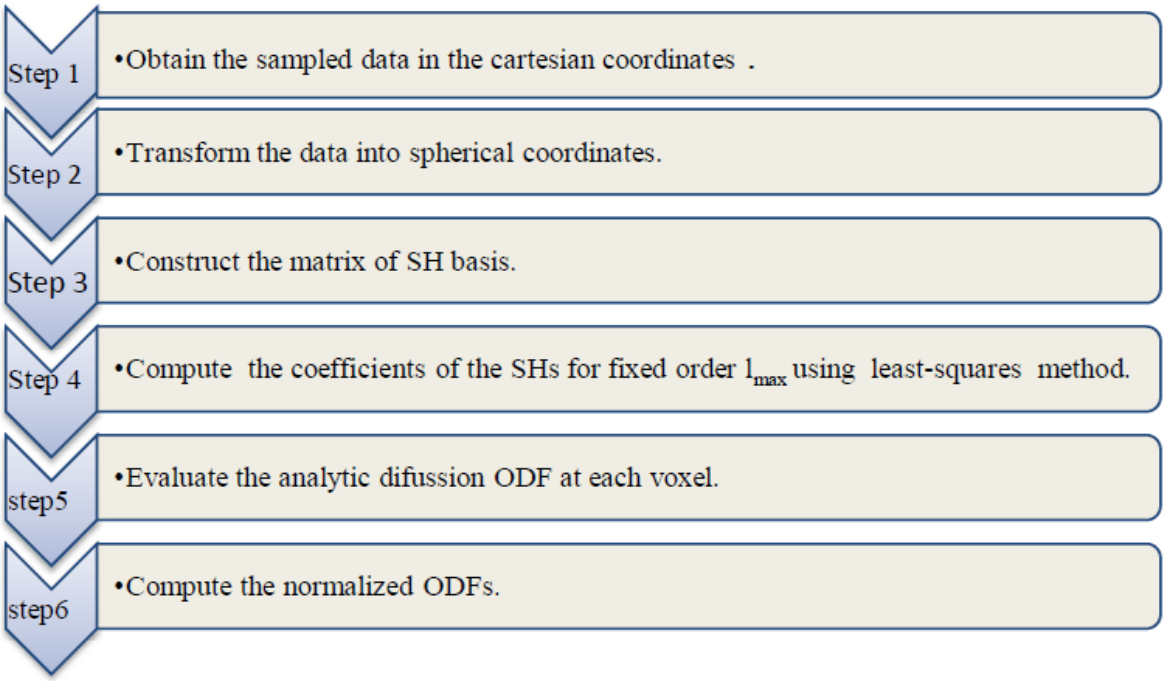

Figure 2.6: Brief summary of the QBI reconstruction method.

2.2.2.3 Spherical Deconvolution

Instead of recovering an approximation based on dODF, Spherical Deconvolution (SD (Tournier *et al.*, 2004)) aims to recover the fiber Orientation Density Function (fODF) directly. The idea behind SD is to consider the measured HARDI signal S as the sum of different fiber orientation distributions F within the same voxel, each convolved with the response function produced by a single-fiber orientation R as presented in the following equation:

$$S(\theta, \phi) = F(\theta, \phi) \otimes R(\theta) \tag{2.21}$$

where $R(\theta)$ is an axially symmetric response function of a single coherently oriented fiber population evaluated in spherical coordinates along θ ; $F(\theta, \phi)$ is the fiber Orientation Density Function (fODF) and $S(\theta, \phi)$ is the signal measured.
Figure 2.7 demonstrates this process by showing how a diffusion signal of a crossing of two distinct populations of fibers can be modeled.

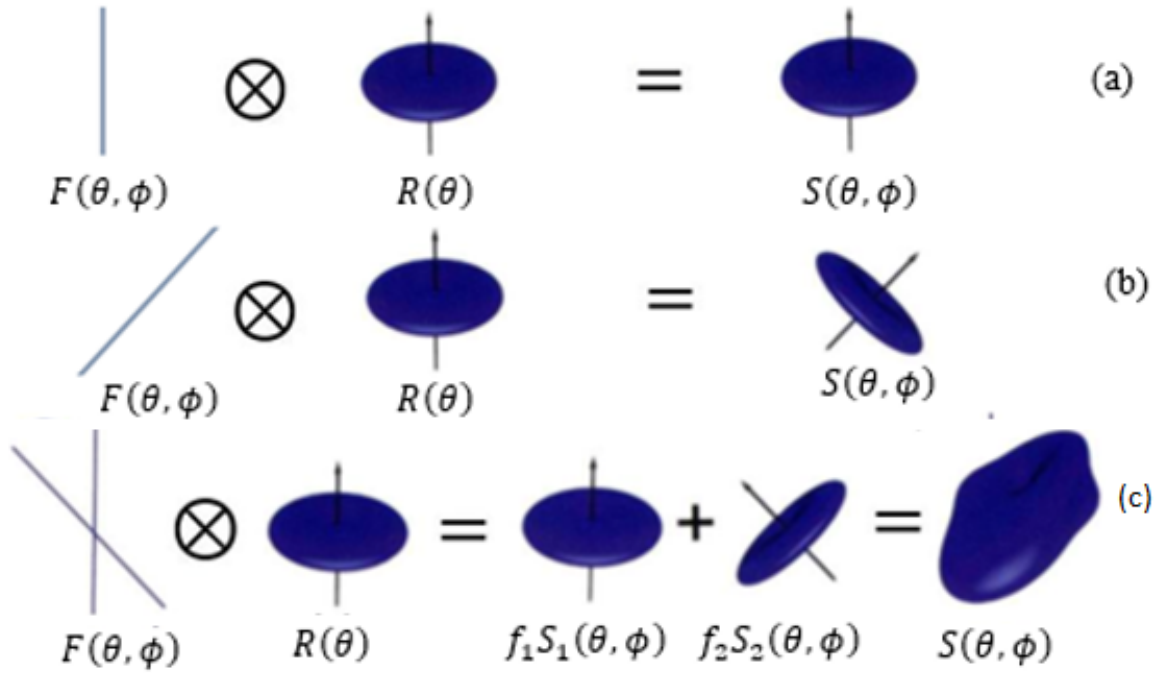

Figure 2.7: Graphial representation of the application of Spherical Deconvolution on crossing fibers. (a) and (b) representation of a single orientation. (c) SD on crossing fibers.

In order to reconstruct the fiber orientations, the measured HARDI signal S is deconvolved with the response function R. F is estimated according to Tournier et al. (Tournier *et al.*, 2007) by averaging the most anisotropic voxels in the brain data. This is a direct

linear operation when all functions are represented in the SH basis (Tournier *et al.*, 2004; Descoteaux, 2008).
Nonetheless, deconvolution techniques are ill-conditioned operations susceptible to noise, resulting in an fODF having negative spurious side-lobes as shown in Figure 2.8. To remove these spurious side-lobes, Tournier at all introduced a non-negativity constraint (Tournier *et al.*, 2007) (hence the name: Constrained Spherical Deconvolution).

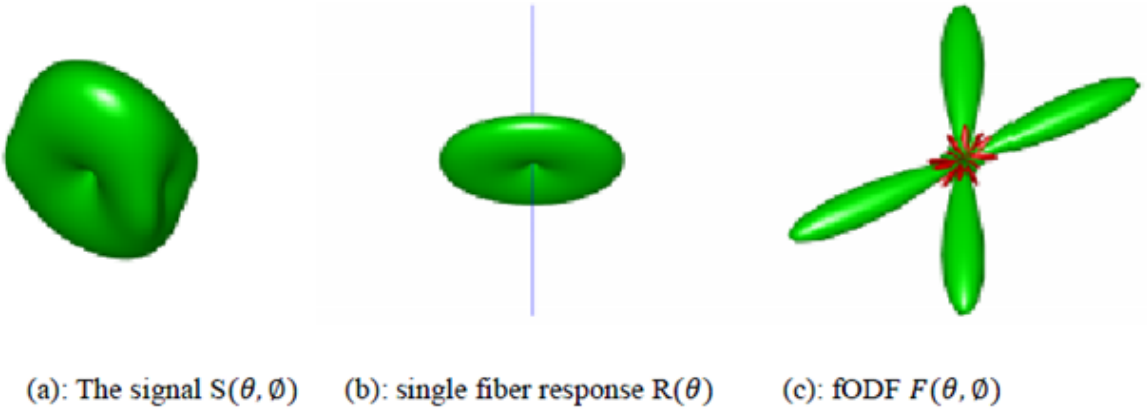

Figure 2.8: Negative spurious side-lobes are created while estimating the fODF using spherical deconvolution.

2.2.2.3.1 Constrained Spherical Deconvolution

Constrained Spherical Deconvolution (CSD) is one variant of SD. It uses the Tikhnov regularization technique (Hess *et al.*, 2006) to reduce the negative values of fODF.

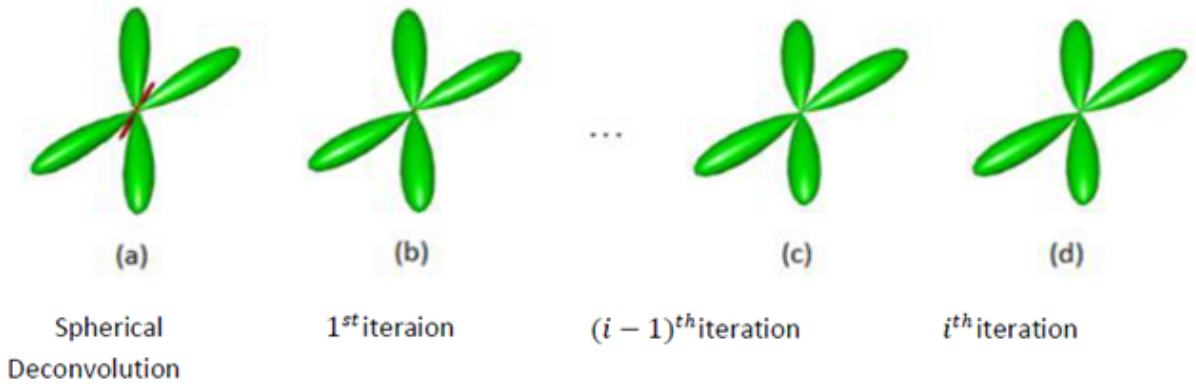

Figure 2.9: Reduction of the negative spurious side-lobes using constrained spherical deconvolution.

The most important steps of CSD are summarized in Figure 2.10, where after the estimation of the fODF, a set of directions is identified where the fODF is negative. By incorporating this information as a Tikhonov constraint, the amplitude of the fODF along

those orientations drops to zero. By solving the Tikhonov problem, an improved version of the fODF is obtained, providing a new set of negative amplitude directions. The process is repeated until convergence is achieved. Figure 2.9 shows the results of CSD, where we can see that by the ith iteration the negative side-lobes where eliminated.

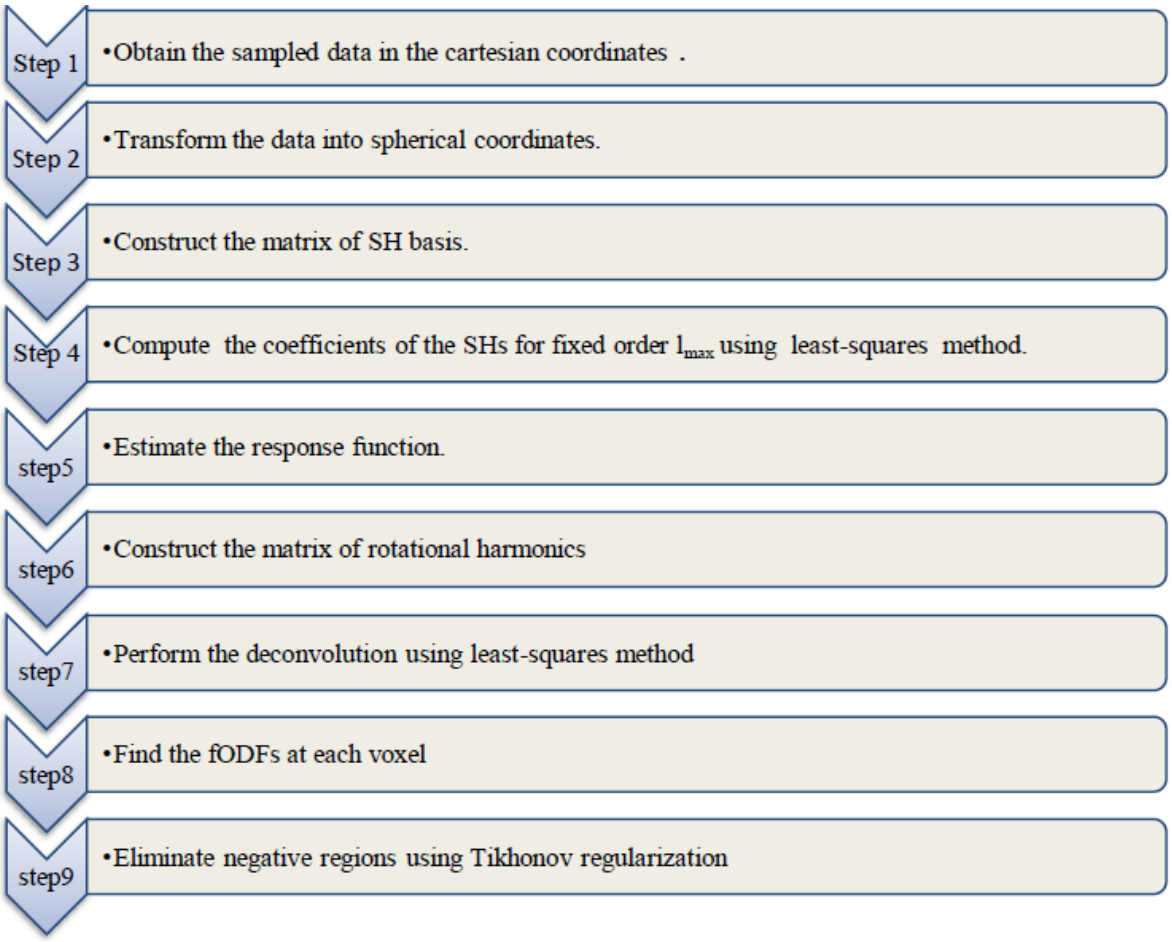

Figure 2.10: Important steps of the CSD reconstruction method.

2.2.2.4 Limitations of HARDI

Although HARDI can overcome the DTI local crossing problem, by discriminating different fiber orientations in a single voxel it still has some limitations. Apart from the long acquisition time which is often too long for clinical application -compared to the DTI technique-, HARDI has some limitations in crossing fiber configuration. Different subvoxel configurations can lead to the same diffusion ODF and Fiber Orientation Density (FOD) profiles as demonstrated in Figure 2.11. In the same imaging voxel, fibers can curve, fan/merge, cross, kiss/bottleneck, or branch/merge, and still produce similar-looking diffusion ODF and FOD profile (Descoteaux, 2015). To date, research groups are addressing these problems, and what these fiber configurations produce on real data remains unknown

and ambiguous (Savadjiev *et al.*, 2008).

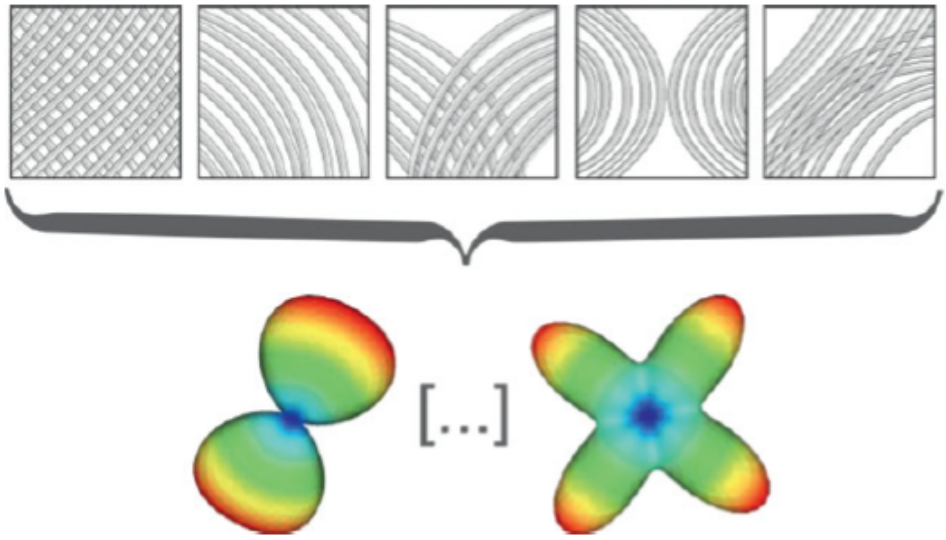

Figure 2.11: HARDI reconstruction limitations. Several ambiguous subvoxel configurations can lead to the same ODF or FOD.(Demi *et al.*, 2014).

2.3 Tractography

Tractography is a general term for methods to reconstruct fiber trajectories in the white matter based on diffusion imaging. It offers a unique possibility to gain insight into the structure of the human brain non-invasively and in vivo. The information won in this manner is not only of high value for visualization of the brain structure and segmentation of the brain into different functional areas, it also provides essential information for neurosurgical planning and investigations of various brain diseases. Since the development of the first algorithms in the late 1990s, many other methods have been proposed in the literature. They can be classified into two main categories: Deterministic and probabilistic algorithms.

2.3.1 Deterministic tractography

In deterministic tractography, a single estimate of fiber orientation is used to determine the direction of the fiber trajectory without taking into account the uncertainty of the chosen pathway. The first fiber tracking approaches were based on DTI, which were later adapted to work with HARDI reconstruction methods, and they all stemmed from the following hypothesis: In each brain voxel, the dominant direction of axonal tracts can be assumed to be parallel to the primary eigenvector of the diffusion tensor. Thus, if the orientation of fibers at each voxel is calculated, these directions are joined to reconstruct

entire pathways and hence brain connections. Although they reconstructed fiber pathways differently, the majority of deterministic methods were based on streamline tractography.

2.3.1.1 Streamline tractography

A streamline through a vector field is any line whose tangent is parallel to the local vector during its entire course. Mathematically, a line can be represented as a 3D space curve $r(s)$, parameterized by its arc length s. In order for a streamline to align with the vector field, the tangent at arc length s, has to be equal to the vector at the corresponding position:

$$\frac{dr(s)}{ds} = v[r(s)] \tag{2.22}$$

where r(s) denotes the 3D position along the streamline and v is the 3D vector field. In the case of fiber tractography, the vector field v is chosen to reflect the local fiber orientations that are calculated from the diffusion data. For DTI tractography, v is typically the field of first eigenvectors derived from the diffusion tensor (Conturo *et al.*, 1999; Basser *et al.*, 2000). For tractography methods based on multi-fiber reconstruction algorithms, v typically consists of the dODF (Wedeen *et al.*, 2008; Descoteaux *et al.*, 2009) or fODF orientations along which the probability is highest (Jeurissen *et al.*, 2009), as these orientations are most likely to coincide with the underlying WM fibers.
Note that equation 2.22 is a differential equation that can be solved by means of integration:

$$r(s) = \int_{s_0} v[r(s)]ds \tag{2.23}$$

where $r(s_0) = r_0$ represents the starting point of the streamline which is often referred to as seed point. Formally, streamline tractography can be defined as the process of integrating voxel-wise fiber orientations into fiber pathways. In the next subsection, we will discuss the most common integration methods used in developing streamline tractography algorithms.

2.3.1.2 Integration

2.3.1.2.1 Euler's method

The most intuitive way to perform the numerical integration of equation 2.23 is by starting the procedure at seed point r_0, calculating the corresponding fiber orientation $v(r_0)$, and following that direction for a short distance $\triangle$, which is called the 'step size', to obtain the next point $r_1 = r_0 + v(r_0)\triangle$ on the pathway. This method, known as Euler integration, can reconstruct the entire streamline by iteratively performing this procedure:

$$r_{i+1} = r_i + v(r_i)\triangle \tag{2.24}$$

Note that equation 2.24 assumes that the value $v(r_i)$ is constant during the step size $\triangle$, which will make this method susceptible to overshoot in highly curved regions, especially for larger step sizes.

2.3.1.2.2 Runge-Kutta method

In order to take into account the variations of v between r_i and r_{i+1}, the use of higher order numerical integration schemes has been proposed, such as the fourth-order Runge-Kutta (RK4) scheme:

$$r_{i+1} = r_i + \frac{k_1}{6} + \frac{k_2}{3} + \frac{k_3}{3} + \frac{k_4}{6} \tag{2.25}$$

with

$k_1 = v(r_i)\triangle$

$k_2 = v(r_i + \frac{k_1}{2})\triangle$

$k_3 = v(r_i + \frac{k_2}{2})\triangle$

$k_4 = v(r_i + k_3)\triangle$

Figure 2.12 shows the geometric representation of RK4 integration method. As shown in the figure, the next point, s_{k+1}, is a linear combination of the main direction of the current point (denoted s_k) and that of the other three surrounding points (A, B and C).

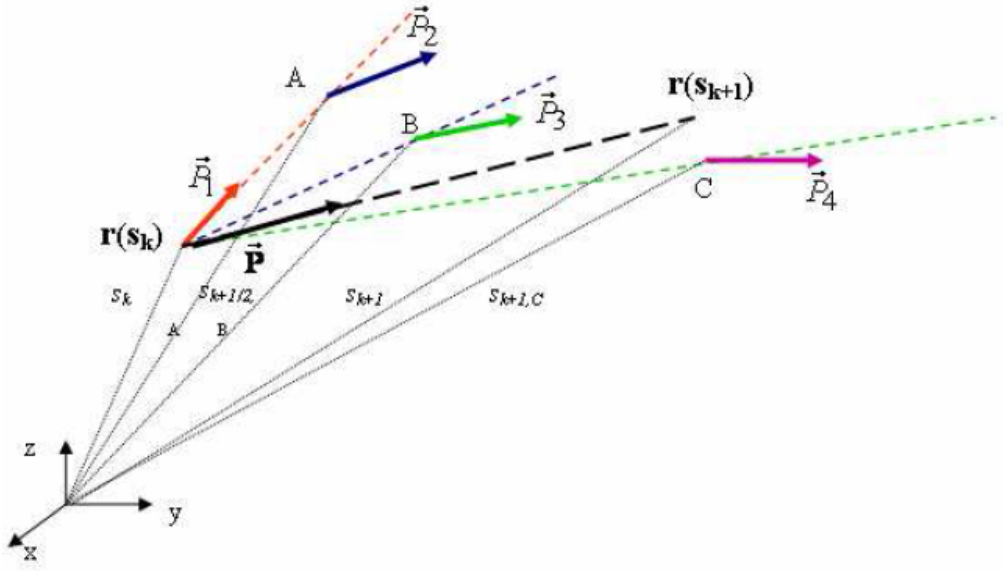

Figure 2.12: Geometric representation of the 4th-order Runge-Kutta method.

An enhanced method combining improved Euler and Runge-Kutta 4th order has been proved to give better results than state-of-the-art tractography algorithms (Cherifi *et al.*, 2018).

2.3.1.3 Interpolation

To minimize errors from integration the vector field needs to be interpolated. The right-hand side of equation 2.22 is defined in continuous space. To progress the streamline correctly, the exact fiber orientation is needed at each position s. The diffusion data, however, is only available on a discrete voxel grid providing only one fiber orientation per imaging voxel.
In the simplest tractography algorithms, streamlines are initiated from user-defined voxels called "seed points" (Figure 2.13). The streamlines follow the primary eigenvector from voxel to voxel in 3 dimensions. When the fiber trajectory reaches the edge of the voxel, the direction of the trajectory is changed to match the primary eigenvector of the next voxel. This method is introduced by Mori (Mori *et al.*, 1999) and is called "Fiber Assignment by Continuous Tracking" or FACT.

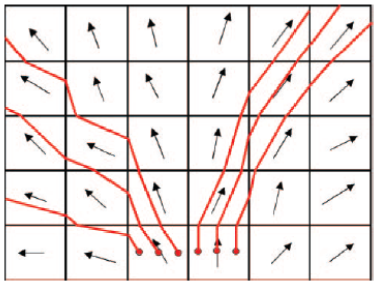

Figure 2.13: Schematic demonstrating the FACT algorithm. Arrows represent primary eigenvectors in each voxel. Red lines are FACT trajectories. From (Mukherjee *et al.*, 2008)

However, this approach leads to a great accumulation of error, which will be then propagated throughout the streamline (Figure 2.14) (Lazar & Alexander, 2003). Therefore we need a method for interpolating the discrete measurements into continuous space. Assuming that fiber orientations contain contributions from all neighboring voxels, the data can be interpolated to gain continuous fiber orientations within a voxel (Figure 2.14). Most algorithms use trilinear interpolation, where the quantity of interest is calculated as a weighted sum from the 8 voxels nearest to the point of interest with the weight of each neighboring voxel determined by their distance to the point of interest.

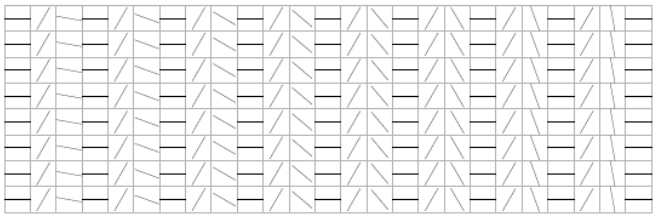

(a) Orientation field

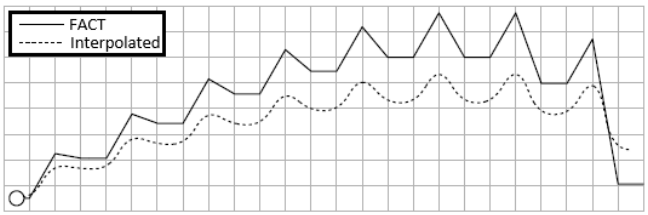

(b) Streamlines

Figure 2.14: Streamlines can be propagated through a voxel with interpolation (interpolated) or without interpolation (FACT) (Jeurissen, 2012).

2.3.1.4 Tensorline tractography

Unlike the method described previously, the Tensor Deflection method TEND, introduced by Lazar (Lazar *et al.*, 2003) uses all of the information contained in the diffusion tensor to determine the direction of the fibers. In this approach, the fiber path does not automatically follow the first eigenvector of a voxel. Rather, the new propagation direction at a given point depends both on the local diffusion tensor D and the tangent on the fiber:

$$\overrightarrow{v}_{out} = D\overrightarrow{v}_{in} \tag{2.26}$$

where v_{in} and v_{out} are respectively "incoming" and "outgoing" vectors (directions) at the current point (Figure 2.15-a). The diffusion tensor D deflects the incoming direction towards the first eigenvector, while limiting the angle of deviation in order to obtain a smoother trajectory. The incoming vector can be defined as a linear combination of the three eigenvectors of the tensor at the current point:

$$\overrightarrow{v}_{in} = \beta_1\overrightarrow{v}_1 + \beta_2\overrightarrow{v}_2 + \beta_3\overrightarrow{v}_3 \tag{2.27}$$

where β1, β2 and β3 are the relative weights of the three eigenvectors.
Using the diagonalized form of the tensor D and substituting the expression of v_{in} in equation 2.26, we obtain:

$$\overrightarrow{v}_{out} = \lambda_1\left(\beta_1\overrightarrow{v}_1 + \frac{\lambda_2}{\lambda_1}\beta_2\overrightarrow{v}_2 + \frac{\lambda_3}{\lambda_1}\beta_3\overrightarrow{v}_3\right) \tag{2.28}$$

From this equation, it is possible to deduce several cases (Figure 2.15-b and 2.15-c):

- If the diffusion is anisotropic ($\lambda_1 \gg \lambda_2 \sim \lambda_3$), the outgoing vector will be diverted according to the direction of the main eigenvector v_1: $\overrightarrow{v}_{out} \backsimeq \lambda_1 \beta_1 \overrightarrow{v}_1$
- If diffusion is mainly in a plane ($\lambda_1 = \lambda_2 \gg \lambda_3$), the outgoing vector will be: $\overrightarrow{v}_{out} \backsimeq \lambda_1(\beta_1 \overrightarrow{v}_1 + \beta_2 \overrightarrow{v}_2)$. In this case, the first and the second eigenvectors both participate in the determination of the new direction. If the Incoming vector is parallel to the diffusion plane, it will hardly be deviated.
- In the case of an isotropic diffusion ($\lambda_1 = \lambda_2 = \lambda_3$), the incoming vector will be almost not modified: $\overrightarrow{v}_{out} = \lambda_1(\beta_1 \overrightarrow{v}_1 + \beta_2 \overrightarrow{v}_2 + \beta_3 \overrightarrow{v}_3)$.

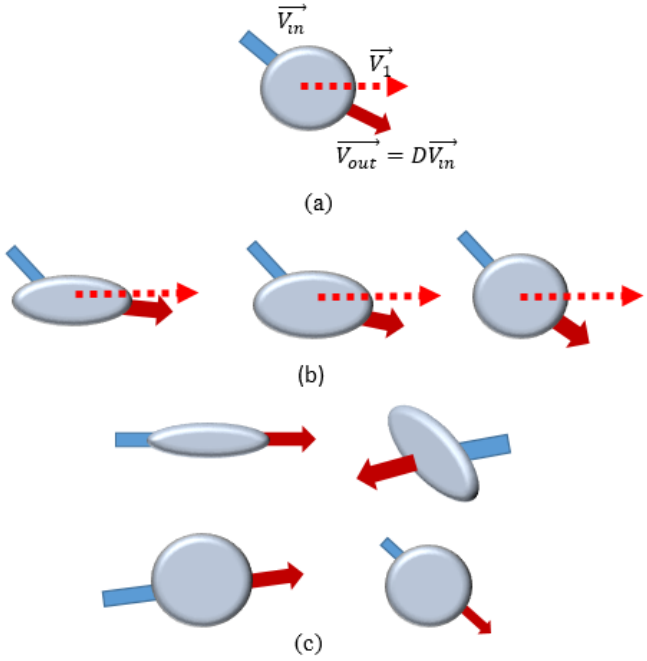

Figure 2.15: : Illustration of the TEND method. (a) Deviation of the incoming vector (blue) by the tensor D (represented by its ellipsoid). The outgoing vector is shown in red. (b) Illustration of the deviation of the incoming vector as a function of the shape of the diffusion tensor. For tensors with high anisotropy (left), the incoming vector is diverted to the main eigenvector v1. The amplitude of the deviation decreases with the anisotropy (from left to right). (c) Illustration of 4 cases for which there will be no deviation: the incoming vector is perpendicular (top right), parallel (top left) to the main eigenvector, when the incoming vector is parallel to the diffusion plane (ellipsoid in the form of slab) (bottom left) and finally in the case of a spherical ellipsoid (lower right).

The author also proposed to calculate v_{out} as the following linear combination:

$$\overrightarrow{v}_{out} = f\overrightarrow{v}_1 + (1-f)((1-g)\overrightarrow{v}_{in} + gD\overrightarrow{v}_{in}) \tag{2.29}$$

where f and g are user defined parameters between 0 and 1 to weight the influence of the first eigenvector, v_1, and the prior tracking direction v_{in}, respectively. This method reconstructs "smoother" fibers because it takes into account the current main direction v1, but suffers from the problem of heuristically choosing values for parameters f and g.

2.3.1.5 Seed points selection

The starting points of tractography algorithms are called "seed points" which define a specific 'region of interest' (ROI). The choice of seeds does not really depend on the method of tractography used. Nevertheless, for deterministic methods, there are two main ways of determining these seeds: The first consists of user-defined ROIs. This method requires anatomical knowledge and is subject to inter-operator variability. In the second, a minimum threshold of FA makes it possible to automatically select the voxels where the diffusion is highly anisotropic. Each chosen voxel is associated with either a single seed point, placed in the center of the voxel, or several seed points, which is accomplished by sub-sampling the voxels by means of a grid of a dimension defined beforehand (Nimsky *et al.*, 2006).

2.3.1.6 Tract termination

Since the propagation of the fibers cannot continue indefinitely, one or more criteria for stopping the tractography algorithm must be defined. Two such criteria are commonly used: a threshold on diffusion anisotropy and a curvature threshold. For example, in DTI tractography it is common to stop a streamline when the FA falls below a certain threshold value (typically FA < 0.2). The rationale behind this criterion is that in regions with low FA values the uncertainty of the fiber orientation is high. Terminating the streamline at such a point prevents the trajectory from acquiring high directional errors. Further, low FA values indicate that the trajectory has left white matter and entered gray matter where no fibers exist. For tractography methods based on multi-fiber reconstruction algorithms, tracking is usually terminated when the dODF or fODF amplitudes along the current tracking orientation fall below a certain threshold (Descoteaux *et al.*, 2009; Jeurissen *et al.*, 2011). The curvature threshold imposes a maximum local curvature of the tract: if the angle between two successive steps is above a predefined threshold, the tract is terminated. Since it is unusual to find bends in the white matter bundles that have radii of curvature on the scale of an imaging voxel, any sudden change in trajectory is likely to be caused by artifacts such as noise or due to errors made in previous steps.

2.3.1.7 Limitations

Deterministic streamline tractography is susceptible to three main sources of errors (Johansen-Berg & Behrens, 2013). First, Diffusion-Weighted Imaging (DWI) is susceptible to imaging noise, leading to a poor estimation of the dominant diffusion directions used in streamline tractography. Second, the microscopic anatomy of WM is bound to be more complex than what can be represented by the fiber reconstruction model. As such, streamline tractography is subject to modeling errors. This is especially true for tractography algorithms using the diffusion tensor model, which cannot resolve multiple fiber orientations inside one voxel. Finally, as mentioned previously, deterministic tractography is subject to integration errors.

2.3.2 Probabilistic tractography

Deterministic tractography is highly sensitive to uncertainty in orientation, due to measurement noise and physiologic motion (Anderson, 2001). A single erroneous direction can result in a non-existing unreliable tract due to the accumulation of error and its propagation, with no possibility to derive reliability from the resulting tracts.
In order to overcome this issue, probabilistic tractography algorithms have been developed. These algorithms provide uncertainty information when reconstructing streamlines by estimating probability distribution in each voxel (Behrens *et al.*, 2007; Parker & Alexander, 2005). The width of this distribution is proportional to its uncertainty, whereas its mean corresponds to the orientation used in deterministic tractography. Once the uncertainty it must be propagated along the fibers. This is done at the expense of a much higher computational time.

2.3.2.1 Characterizing Uncertainty

Designing probabilistic tractography algorithms starts by estimating the uncertainty of fiber trajectories, also known as uncertainty ODF (uODF).
Uncertainty ODF doesn't quantify a physical property as opposed to dODF and fODF, it rather represents the made assumptions about the microstructure of the tissue. The uncertainty of fibers orientation is defined as a probability of the fiber orientation to exist within specific area of the surface of a sphere. Figure 2.16 depicts how uODF represents uncertainty through the radius of the present cones.

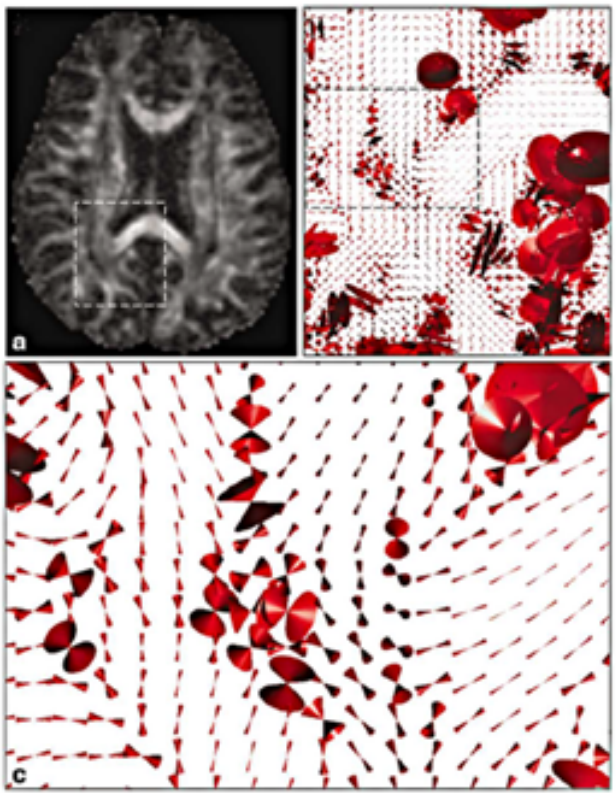

Figure 2.16: Cones of uncertainty (showing the 95% confidence angle) at the level of the splenium of the corpus callosum. a: Fractional anisotropy. b: Cones of uncertainty in the region indicated by the dashed lines in a. This region is further magnified in c. The zoomed area highlights a region where fibers cross and the uncertainty in 1 is large (Jones, 2003).

Small radii indicate regions of one fiber populations, and the bigger these radii get, the more complex the fiber configuration gets.
To estimate the uODF, several techniques were developed, we explore the most used one here which is the Bootstrapping technique.

2.3.2.2 Bootstrapping technique

This approach estimates the uODF by taking multiple repetitions of the original data, reconstruct the diffusion direction by randomly using a subset of data set and treat the repeated measurements as samples from the uODF (Jones, 2003) as illustrated by Figure 2.17. This method presents some drawbacks, regarding the large acquisition load and underestimation of the uncertainty due to the fact that the samples are not independent.

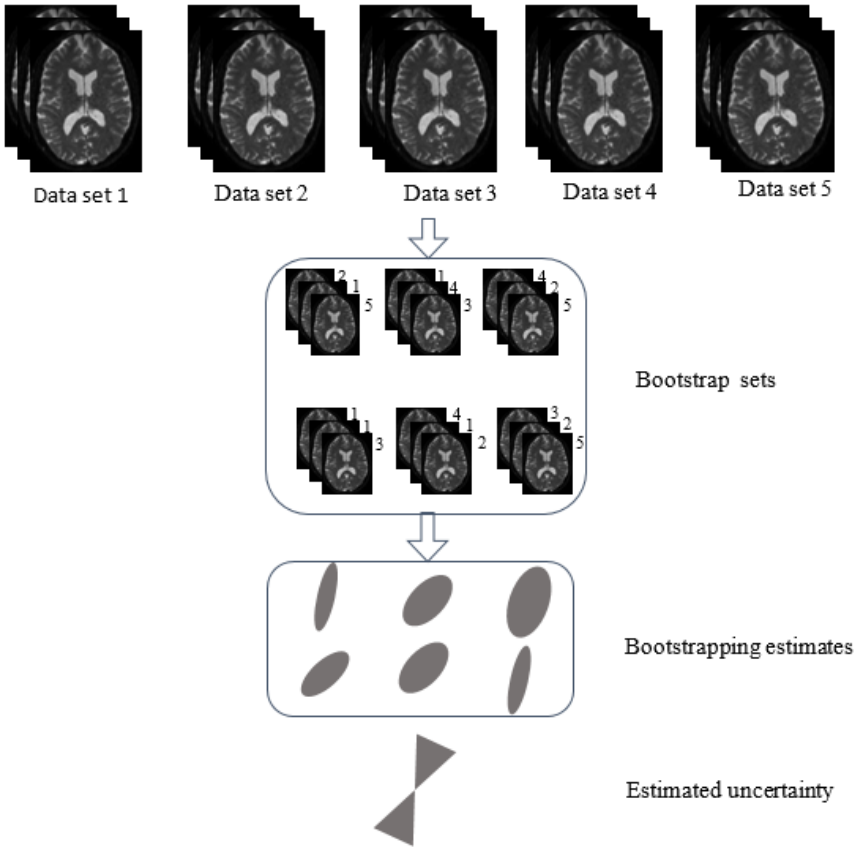

Figure 2.17: Illustration of the bootstrapping technique.

2.3.2.3 Uncertainty propagation

In deterministic tractography, streamlines integrate the fiber trajectory by aligning with the maximum diffusion direction. In Probabilistic tractography this is no longer valid, since there exists an infinite number of possible orientation with their corresponding probability. Samples from the computed uODF are rather drawn to estimate and generate the possible pathways.

The pathway is reconstructed by constantly advancing the trajectory starting from a seed point along a sample direction drawn from the uODF until the stopping criterion is met. The output of this procedure is a one possible streamline. The whole probability density function can be reproduced by advancing the trajectory starting from the same seed point along a different sample direction many times.

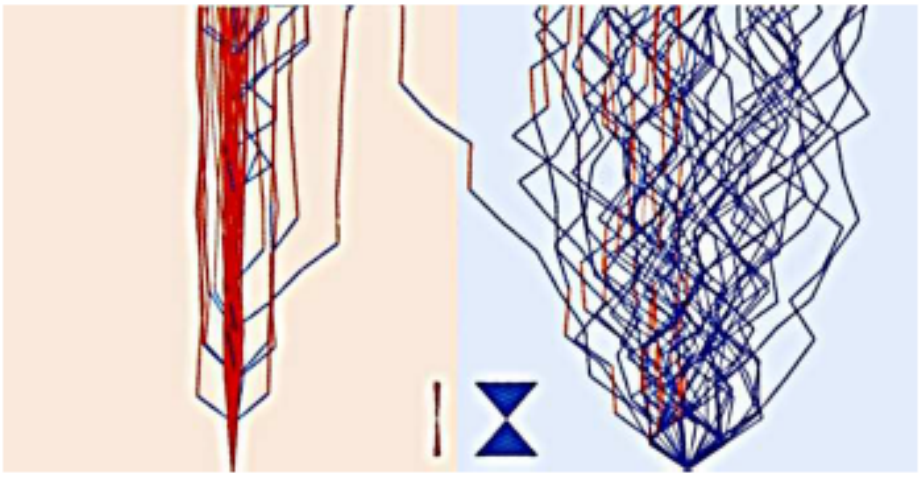

Figure 2.18: Propagation of streamlines with low (red voxel) and high uncertainty (blue voxel). Sample streamlines are started from the bottom of each voxel. Samples are drawn from the uODF and the streamline is advanced one step. The illustrated step size is one tenth of a voxel. Image adopted from (Johansen-Berg & Behrens, 2013).

2.3.3 Tractography algorithms validation

It is important to evaluate the quality of the results of tractography, not only qualitatively, but also be able to quantify the accuracy, reproducibility and reliability (Leemans *et al.*, 2005). The absence of a "golden standard" makes it difficult to validate results of fiber tracking. Subcortical electrical stimulation remains the only reference for validation. However, this technique is mainly reserved for patients with tumors during tumor excision. Nevertheless, the evaluation of the different tractography methods can be performed on data acquired on phantoms, physical (Lin *et al.*, 2001; Perrin *et al.*, 2005; Pullens *et al.*, 2010) or simulated (Lori *et al.*, 2002; Leemans *et al.*, 2005), by means of the tractometer, which is a tool used to evaluate the end effects on fiber tracts of tractography algorithms among other things (Côté *et al.*, 2013). Another validation approach is to compare tractography results with another imaging modality. For example, it has been demonstrated that functional networks can be mapped using functional MRI at resting state (Raichle *et al.*, 2001; Vincent *et al.*, 2007). These functional networks must, to a certain extent, be linked to an underlying structural connectivity. Studying the relationship between structure and function can only help us understand the architecture of the brain, but can also prove the relevance of tractographic reconstructions.

2.4 Summary

The choice of both the reconstruction method and tractography algorithm depends on several factors, such as the type of the study, the prior information we have on the true connectivity and the type of diffusion data. Each algorithm produces a unique representation of the anatomical connectivity. These facts will be taken into consideration in the next chapter where we will conduct our experimental study.

Chapter 3

Experimental Part

3.1 Introduction

The main objective of this chapter is to examine some cases of patients with astrocytomas through the application of reconstruction and tractography methods previously introduced, in order to investigate how these tumors affect the surrounding WM tracts. We will also explore the differences between the results obtained using different reconstruction techniques. Finally, a quantitative comparison between the left and right hemispheres will be performed on normal and clinical cases.

3.2 Software environment

3.2.1 Computer

The experiment was conducted on Lenovo PC, equipped with Windows 8.1 Professional 64 bits Operating System. The memory capacity (RAM) 4.00 Go. The processor Intel(R) Core(TM) i3 CPU @ 2.00 GHz.

3.2.2 Dipy

Diffusion Imaging in Python (Dipy) is a free and open source software project for the analysis of data from diffusion MRI experiments. Dipy is the first collective effort to create an open-source diffusion MRI analysis library using the Python language. It implements a broad range of algorithms for denoising, registration, reconstruction, tracking, clustering, visualization, and statistical analysis of MRI data.
Dipy takes full advantage of the scientific computing tools in Python, and is built on top of high-performance Python libraries (Table 3.1).

Dipy's main sub-modules (see Figure 3.1) are core, reconst, tracking, viz, io, align, data, sims and segment.

Python	(core language) It is a general purpose, object-oriented programming language which was designed with an emphasis on code readability. This emphasis allows scientists who are not trained as software engineers to understand the computational steps taken during the analysis and to extend the software easily.
Numpy	The core structure of this library is an implementation of an N-dimensional array class. Numpy arrays are used for representing numerical data in Python and enable efficient numerical computations through the use of vectorized operations, by avoiding data copying, and by minimizing the number of operations performed. Numpy is also used for matrix, tensor and linear algebra operations.
Scipy	It used for non-linear optimization and other volumetric operations.
Cython	It converts Python code into Python C extensions by interpreting static type declarations. It is used in rare cases when both standard Python and Numpy/Scipy are not fast enough for the task at hand.
Nibabel	It is a package for loading and saving medical imaging file formats.
VTK	Stands for Visualization Toolkit, and is an open-source, freely available software system for 3D computer graphics, image processing, and visualization. It consists of a C++ class library and several interpreted interface layers including Tcl/Tk, Java, and Python. VTK supports a wide variety of visualization algorithms including scalar, vector, tensor, texture, and volumetric methods.
Matplotlib	It is a Python 2D plotting library which produces publication quality figures in a variety of hardcopy formats and interactive environments across platforms.
IPython	It is used as an interactive Python shell for calling and debugging scripts.

Table 3.1: Brief summary of DIPY's dependencies.

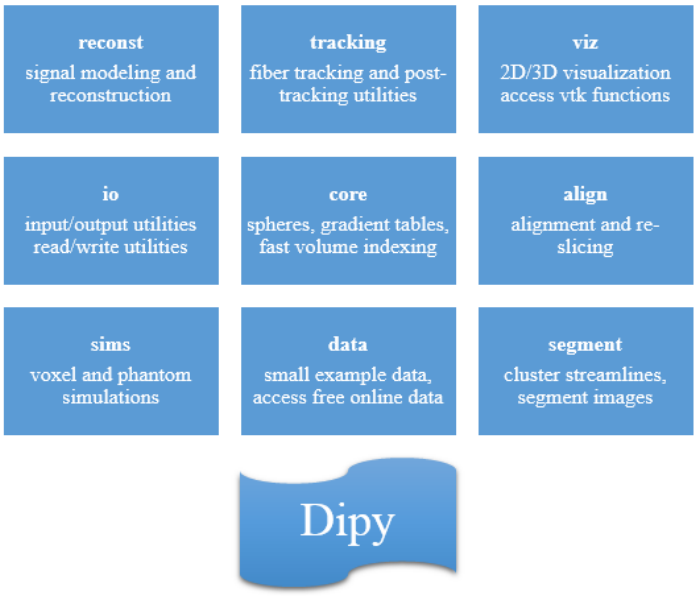

Figure 3.1: DIPY's sub-modules.

3.2.3 MI-Brain

MI-Brain (Medical Imaging Brain) is a software dedicated to the visualization, processing and analysis of diffusion images developed by the Canadian company Imeka (Figure 3.2) in 2015. MI-Brain allows you to visualize, edit, analyze images and perform a real-time tractography of nerve fiber bundles from diffusion MRI images.

Figure 3.2: Imeka's logo.

Among the most important features of MI-Brain, we have:

- The possibility to stack the images (open several images at the same time and superimpose them).
- The treatment of a multitude of file formats: fiber bundle file, DWI, DICOM, NIfti, PGN, TIFF, GIF, BMP, JPEG.
- The segmentation of specific nerve fiber bundles from one region of interest (ROI) to another.
- The display of fibers having a minimum and / or a maximum of length (in mm).

3.3 Analysis steps

3.3.1 Dataset

In order to conduct this study, a dataset entitled "A neuroimaging dataset of brain tumour patients" created by Edinburgh Experimental Cancer Medicine Centre and available at the UK Data Archive was used (Pernet *et al.*, 2016). The dataset encloses Brain imaging data from 22 patients with brain tumor and includes T1, T2, DTI and functional MRI data alongside clinical information.
The data were acquired on a GE Signa HDxt 1.5 T scanner with an 8 channel phased-array head coil at the Brain Research Imaging Center, University of Edinburgh, UK. The parameters of interest used to acquire the data are:

- T1 (coronal acquisition, field- of-view 256 × 26 mm, slice thickness 1.3 mm, 156 slices, acquisition matrix 256 × 265, TR = 10s, TE = 4 s, and inverstion time (T1) 500ms).

- T2 (spin-echo echo-planar imaging volume with a field of view 256 × 26 mm, slice thickness 2 mm, 72 axial slices, acquisition matrix 128 × 128, TR = 16,5 s, TE = 98 ms).
- Diffusion Tensor Imaging (64 directions, b = 1000 s/mm^2; plus seven T2-weighted (b =0 s/mm^2 single-shot spin-echo echo-planar imaging volumes with a field of view 256 × 26 mm, slice thickness 2 mm, 72 axial slices, acquisition matrix 128 × 128, TR = 16,5 s, TE = 98 ms).

The 22 patients have a confirmed presence of brain tumors, though they differ in their type, location and size, the ones used for this study all have different levels of Astrocytoma.

3.3.2 Data preprocessing

3.3.2.1 Format conversion

The raw data provided by the dataset in DICOM format had to be converted to the 4D NIfTI1 format which is the most commonly used format in diffusion MRI. The conversion was performed using a MATLAB code.
Once the 4D NIfTI1 file is ready, the pre-processing step is performed on Dipy.

3.3.2.2 Loading and Background removal

The loading of the 4D NIfTI1 file ("myfile.nii.gz") is realized using the NiBabel package by creating an object "img" holding all information contained in the used file while the fdwi holds its path.

```
fdwi = join(dname, 'myfile.nii.gz')
import nibabel as nib
img = nib.load(fdwi)
```

Other than the 4D NIfTI1 file, the bval and bvec files need to be imported. The former is a 1× N array containing the b values used, whereas the later holds the values for diffusion-sensitizing magnetic field gradients also known as the b-vectors. These files are used to construct the Gradient Table (gtab) needed for the reconstruction and analysis of DTI later.

```
fbval = join(dname, 'b1000.bval')
fbvec = join(dname, 'bvecs.bvec')
from dipy.io import read_bvals_bvecs
bvals, bvecs = read_bvals_bvecs(fbval, fbvec)

from dipy.core.gradients import gradient_table
gtab = gradient_table(bvals, bvecs)
```

For better reconstruction and tractography results, the background needs to be removed from the brain by applying a median filter followed by Otsu's method. This is done using the median_otsu function whose output are shown in Figure 3.3 - D.

```
from dipy.segment.mask import median_otsu
maskdata, mask = median_otsu(data, 4, 4, False,
                             vol_idx=range(10, 40), dilate=2)
```

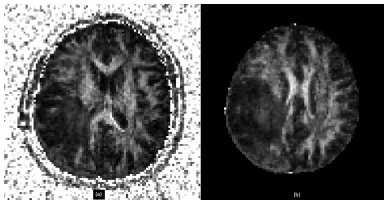

Figure 3.3: Visualization of the extracted brain using median_otsu. (a) The noisy FA image. (b) The filtered FA image.

3.3.3 Data processing

The preprocessed data are ready to be used for reconstruction. To better investigate the effect of the brain tumors on the white matter micro-structure, two different modeling techniques for reconstruction were used: DTI and CSD.

3.3.3.1 Reconstruction

- DTI reconstruction:

DTI analysis begins with the estimation of the tensor at each voxel. This is achieved by firstly importing the diffusion tensor model class and initialize a TensorModel class instance tensor_model by using the previously generated gtab and selecting the fitting method (in this case) Weighted Leas Square.
The analysis is started by passing the data to the fit method of the TensorModel class.

```
from dipy.reconst.dti import TensorModel
tensor_model = TensorModel(gtab, fit_method='WLS')
tensor_fit = tensor_model.fit(data, mask)
```

Once the fit is achieved, we extract peaks from model in order to set the stage for the tractography later. This is achieved by the use of the utility function peaks_from_model.

```
from dipy.direction import peaks_from_model
dti_peaks = peaks_from_model(model=tensor_model,
                             data=data,
                             sphere=sphere,
                             mask=mask,
                             relative_peak_threshold=.5,
                             min_separation_angle=25,
                             parallel=False)
```

- CSD reconstruction:

A crucial step prior to CSD analysis is the estimation of the response. This is done by using the auto_response function which estimates the response function for voxels of high Fractional Anisotropy (FA> 0.7) from a region of interest (Corpus Callosum) of a predetermined radius in the center of the volume.

```
from dipy.reconst.csdeconv import (ConstrainedSphericalDeconvModel,
                                   auto_response)

response, ratio = auto_response(gtab, data, roi_radius=10, fa_thr=0.7)
```

The quality of the estimated response function can be confirmed by visualizing it or by displaying its value (Figure 3.4).

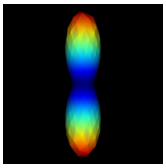

Figure 3.4: Visualization of the estimated response.

After estimating the response, we can use the CSD method implemented in Dipy to create an instance of the model.

```
csd_model = ConstrainedSphericalDeconvModel(gtab, response)
```

The extraction of the peaks from the resulting model is done using the same previously introduced function peaks_from_model.

3.3.3.2 Fiber tractography

After recovering the peaks and directions from model, tracking can be achieved by setting a stopping criteria. One stopping criterion is related to the Fractional Anisotropy, where it's specified that the tracking should stop for regions of low FA.
In order to generate the streamlines, the seed points should be specified beforehand. This is done by means of random_seeds_from_mask method which places randomly distributed seeds in voxels specified by a previously determined mask.
The streamlines are generated using EuDX implemented in the method LocalTracking. The resulting tractography is saved in a *trk file which would be used for visualization. To visualize the results of the tractography, several software programs can be used. In our study we used MI-Brain.

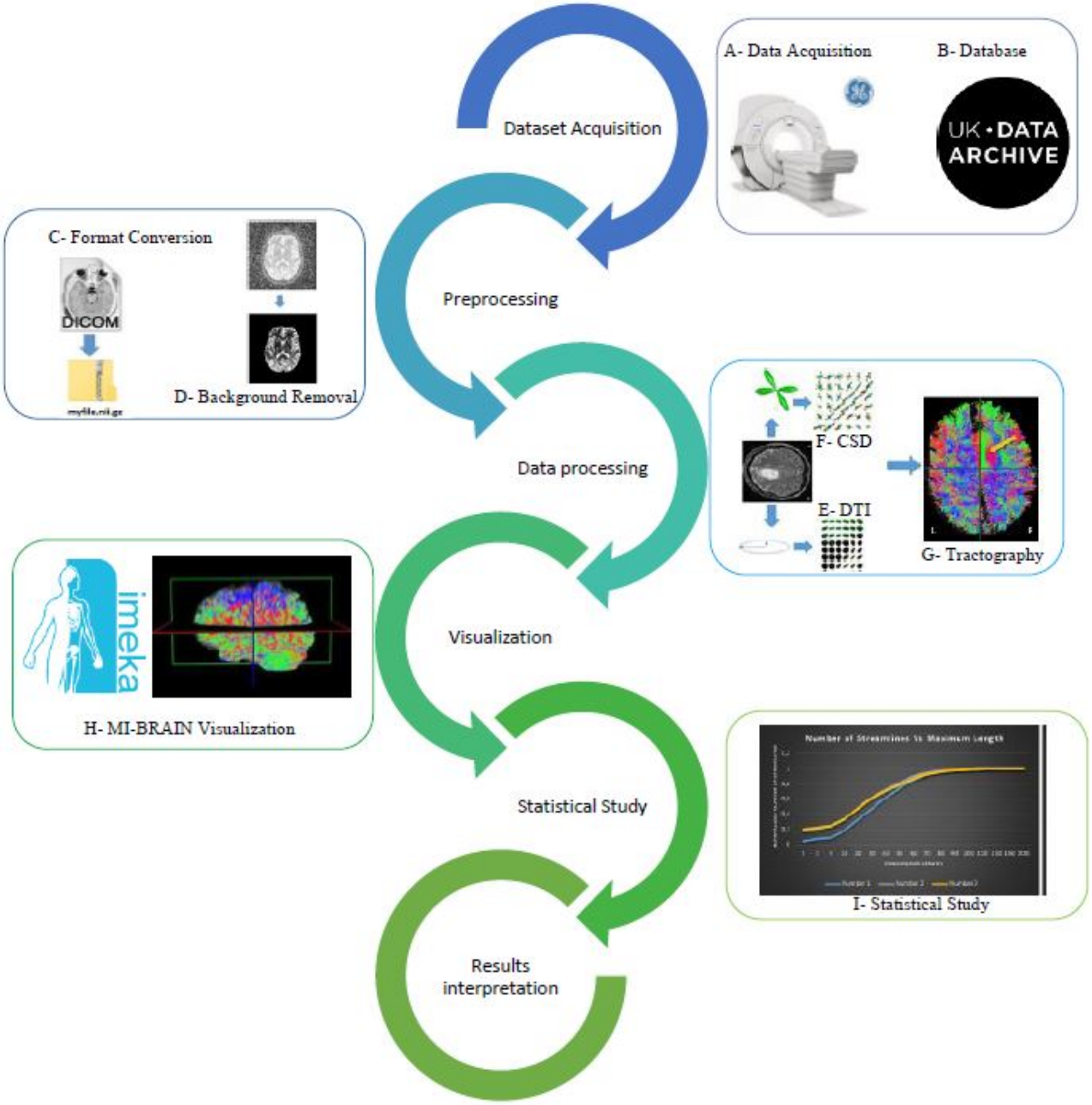

Figure 3.5: In order to perform a diffusion MRI study, the first step is data acquisition (A) from a public database (B). The data should undergo quality control, preprocessing, including format conversion (C), and background removal (D). Before further analysis, tensors (E) or fODFs (F) need to be estimated. The fibers are then reconstructed using tractography technique (G). MI-Brain software was used to visualize and manipulate the obtained tractograms (H), in order to illustrate the results by performing a quantitative analysis (I). Finally, results interpretation should be made with extreme caution.

3.4 Clinical cases study using CSD-based tractography

We used the data of three patients with differing grades of astrocytomas. The following table shows information about the volume of the major parts of the brain along with the tumor.

	GM	WM	Tumor	CSF
Case 1	0,6016713	0,4441813	0,1124203	0,2053155
Case 2	0,5834562	0,3857222	0,05487587	0,1544075
Case 3	0,6495395	0,4648716	0,02123101	0,3508827

Table 3.2: Table displaying the volumes (liter).

3.4.1 Cases presentation

Case 1:

A 40-year-old female presented with right glioblastoma. The MRI examination revealed the tumor in the right primary motor area. The FA map showed decreased intra-lesional FA value, indicating the infiltration and destruction of WM tracts. The color coded map (RGB map) showed complete destruction of the WM tracts of the right superior longitudinal fasciculus (SLF) fibers. 3D tractography of the right corticospinal tract (CST) reveals intact but slightly deviated fibers. The coronal slice of the RGB map shows the disruption of the right arcuate fasciculus (AF) fibers. Intact left-sided AF fibers are shown for comparison. 3D tractography of the corpus callosum (CC) shows the primary motor region fibers destructed. Left intact CC is shown for comparison (Figure 3.6).

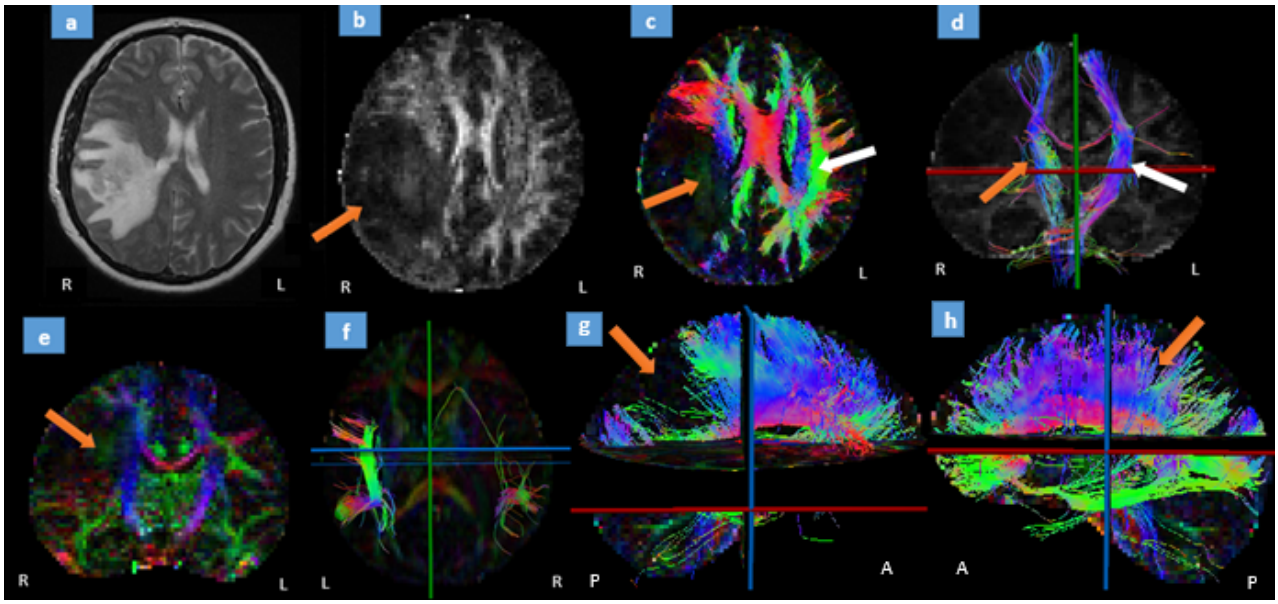

Figure 3.6: **A 40-year-old female with right glioblastoma** - T2-weighted image (a) shows the tumor in right primary motor area. Fractional anisotropy (FA) map (b) shows an intralesional decreased FA (arrow). Color-coded map (c) shows the intralesional white matter fibers of right superior longitudinal fasiculus (SLF) destructed (orange arrow). The left SLF (white arrow) is intact and shown for comparison. 3D fiber tractography (d) shows blue-colored right CST (arrow) slightly deviated compared to the left CST (white arrow). Coronal slice color-coded map (e) shows the disruption of right arcuate fasciculus (AF) (arrow). The 3D fiber tractography of right AF is shown in (f) along with the intact left AF for comparison. The 3D fiber tractography (g) of right corpus callosum (CC) shows the destructed fibers. The left intact CC (h) is shown for comparison. A: Anterior. P: Posterior. R: Right. L: Left.

Case 2:

A 26-year-old female presented with anaplastic Astrocytoma (Astrocytoma grade III). MRI showed the tumor in the right supplementary motor area. FA map shows decreased FA value in the tumoral region. 3D whole brain tractography showed a complete destruction of WM fibers in the anterior midBody and the rostralBody of the corpus callosum (CC) which connects with the premotor and supplementary motor areas. Left and right sagittal 3D tractography views of CC are shown for comparison (Figure 3.7).

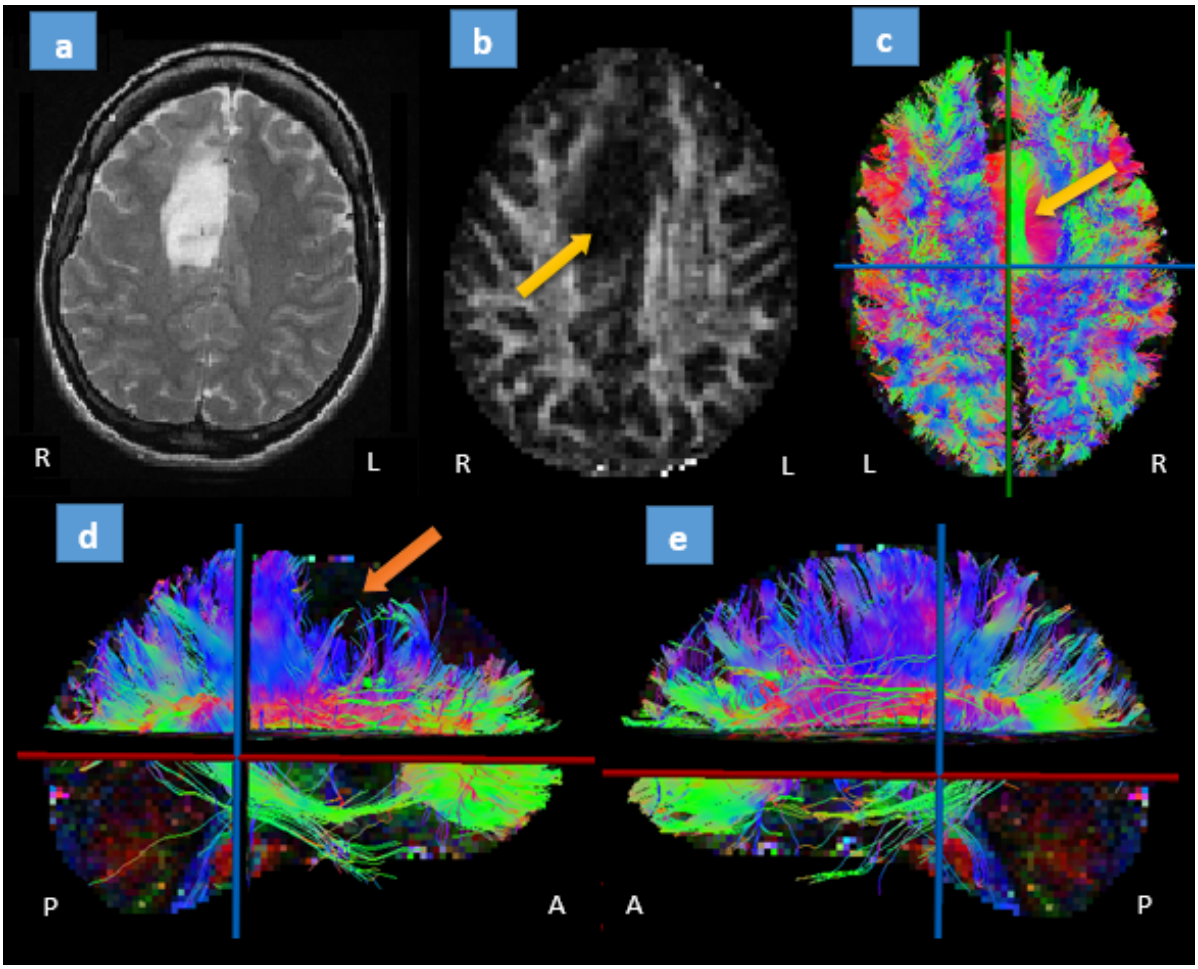

Figure 3.7: **A 26-year-old female with Astrocytoma grade III** - T2-weighted image (a) shows the tumor in right supplementary motor area. Fractional anisotropy (FA) map (b) shows an intralesional decreased FA value (arrow). 3D whole brain tractography (c) shows intralesional white matter tracts destruction (arrow). 3D fiber tractography of CC (d) right sagittal slice shows the disruption of both the anterior midBody and parts of the rostralBody of CC (arrow). 3D fiber tractography of CC (e) left sagittal slice shown for comparison. A: Anterior. P: Posterior. R: Right. L: Left.

Case 3:

This patient has Astrocytoma type II. MRI showed the tumor in Wernicke's area. FA map shows slightly-reduced FA in the affected region. 3D whole brain tractography shows the tumoral region on the left posterior side of the tractogram. 3D tractography initiated in the region of interest shows the displacement of fibers around the surface of the lesion. The intact counterpart on the right hemisphere is shown for comparison (Figure 3.8).

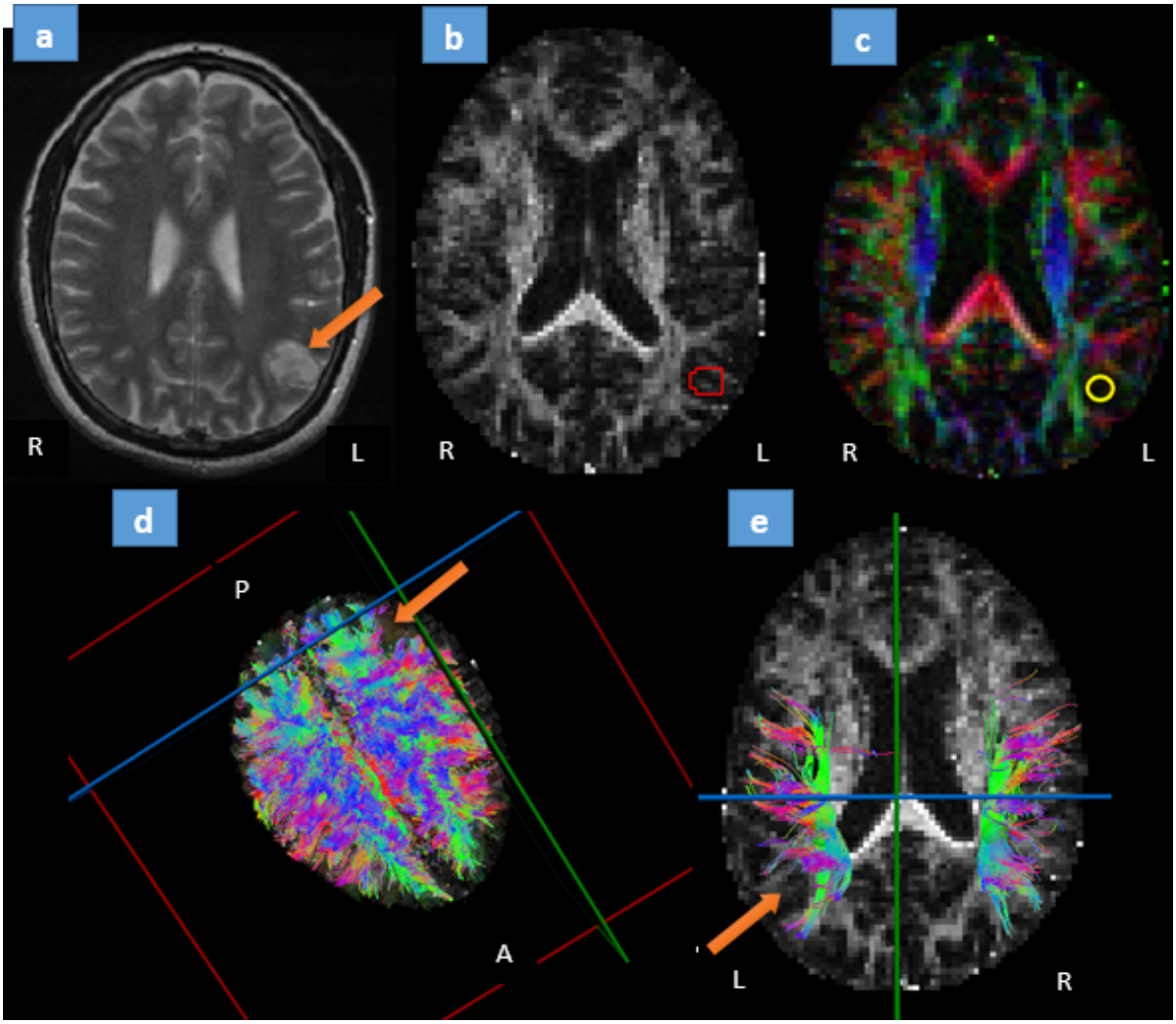

Figure 3.8: **Patient with Astrocytoma grade II** - T2-weighted image (a) shows the tumor in Wernicke's area. Fractional anisotropy (FA) map (b) shows a slight decrease in FA value (red region). The same region is shown in color-coded map (c) (yellow circle). 3D whole brain tractography (d) shows the tumoral region void of white matter tracts (arrow). 3D fiber tractography initiated in ROI (d) on the left hemisphere, shows the displacement of fibers around the tumor. The counterpart tract on the right hemisphere is shown for comparison. A: Anterior. P: Posterior. R: Right. L: Left.

3.4.2 Discussion

The three cases presented above exhibited various behaviors and this can be attributed to the differences in type, location, and size of the tumors, among other factors.
The first case was a glioblastoma, one of the most aggressive grade IV tumors in the brain. From Figure 3.6, we can see that it occupies a large area in the brain, it is also characterized by its massive volume which amounts to 25% of total WM volume (Table 3.2). The decrease in intralesional FA value indicates the loss of directionality due to the alteration of WM pathways. Using tractography, we were able to demonstrate that this tumor led to the complete destruction of some major tracts located in the tumoral region, such as the right superior longitudinal fasciculus (SFL), the right arcuate fasciculus (AF) and the primary motor region fibers of the right side of the corpus callosum (CC). It also caused the displacement of the right corticospinal tract (CST) which was in close relation to lesion.

- One type of relation between tracts and tumors is destruction with displacement, which is most likely exhibited by high-grade tumors that grow in significant brain areas.

The second case represented an anaplastic astrocytoma, a grade III tumor. It represents 14% of the total WM volume (Table 3.2). The distortion of WM tissue integrity is illustrated by the decrease in intralesional FA values. It is further proved by the resulting tractogram which showed the WM tracts infiltrated by the tumor completely destructed.

- One type of relation between tracts and tumors is destruction, which usually leads to the complete disruption of the fibers occupying the same space as the infiltrating tumor.

The last case was an astrocytoma grade II. This tumor was significantly less in volume compared to the previous cases, amounting to only 5% of the total WM volume (Table 3.2). It also showed less significant decrease in the intralesional FA values. Application of tractography on the region of interest revealed the tracts deviated from their original paths.

- One type of relation between tracts and tumors is displacement. This is the most likely type to occur when tumors are small in size and occupy less populated regions.

It should be mentioned that the results found are only proved for the given patients with the specified characteristics.

3.5 Comparison of reconstruction methods

3.5.1 Visual assessment of the tumor using DTI-based tractography

Case 1:

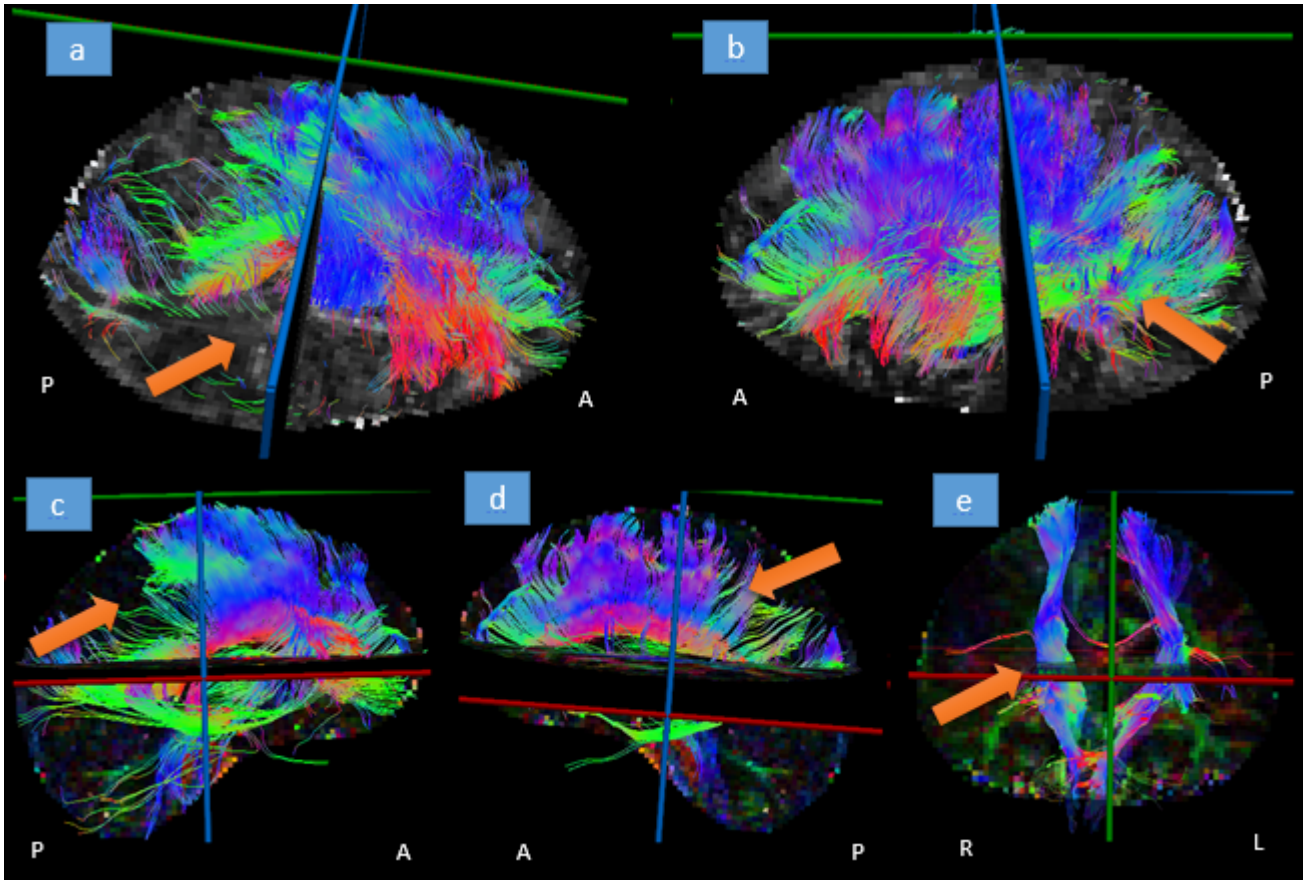

Figure 3.9: **A 40-year-old female with right glioblastoma** - 3D DTI-tratography of (a) whole brain top view of the tumor in the right hemisphere; (b) whole brain top view of intact left hemisphere; (c) corpus callosum (CC) showing the destruction of the right sensory-region fibers (arrow); (d) intact left CC for comparison; (e) corticospinal tract (CST) showing the right CST deviated from its path (arrow) compared to the left intact CST.

Case 2:

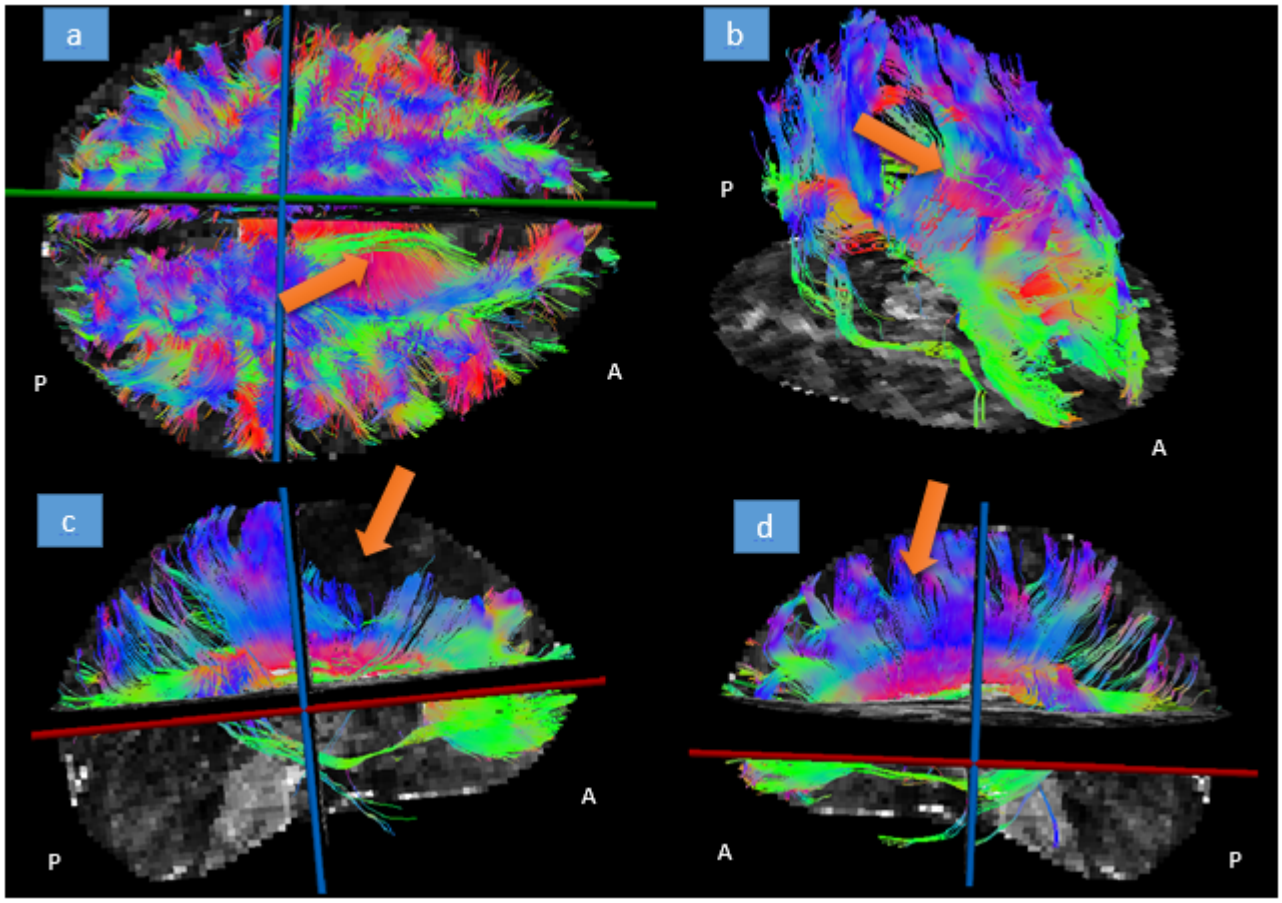

Figure 3.10: **A 26-year-old female with Astrocytoma grade III** - 3D DTI-tratography of (a) whole brain top view of the tumor in the right hemisphere (arrow); (b) corpus callosum (CC) showing the destruction of the right pre-motor and supplementary motor-region fibers (arrow); (c) right CC sagittal view shows the destructed streamlines (d) intact left CC for comparison.

Case 3:

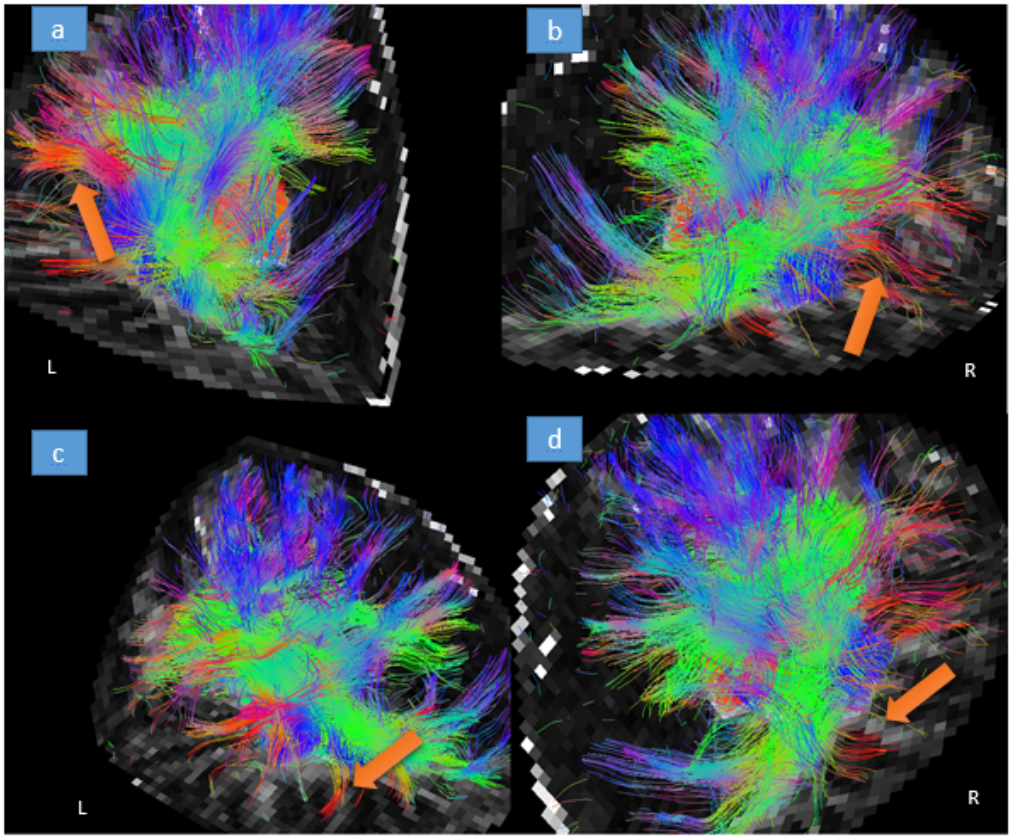

Figure 3.11: **Patient with Astrocytoma grade II** - 3D DTI-tractography of whole brain zoomed in (a) and (c) on the tumoral region showing the compressed and displaced fibers in close relation to tumor (arrow); (b) and (d) on the left intact counterpart for comparison (arrow).

Discussion:

The results found using DTI-based tractography were similar to what CSD-based tractography already disclosed.
The first patient with a grade IV astrocytoma had a massive-sized tumor on the right hemisphere. Some of the tracts located in the same area were completely destructed such as the primary motor region fibers of the corpus callosum. It also revealed the displacement of the right CST. The second patient with a grade III astrocytoma showed the destruction of the fibers located in the anterior midBody and rostralBody of the corpus callosum, which agrees with the earlier findings. Likewise, applying DTI-based tractography on the third patient with a grade II astrocytoma revealed the same alteration which consisted of the displacement of some fibers located within the tumoral region.

We deduce that both DTI- and CSD-based tractography can be used to confirm the presence of tumors and infer their associated alterations.

3.5.2 Voxel-wise assessment of DTI- and CSD-based tractography

We applied both DTI- and CSD-based tractography techniques on the same patient. We isolated the same voxel in both cases to see the difference. We obtained the following results:

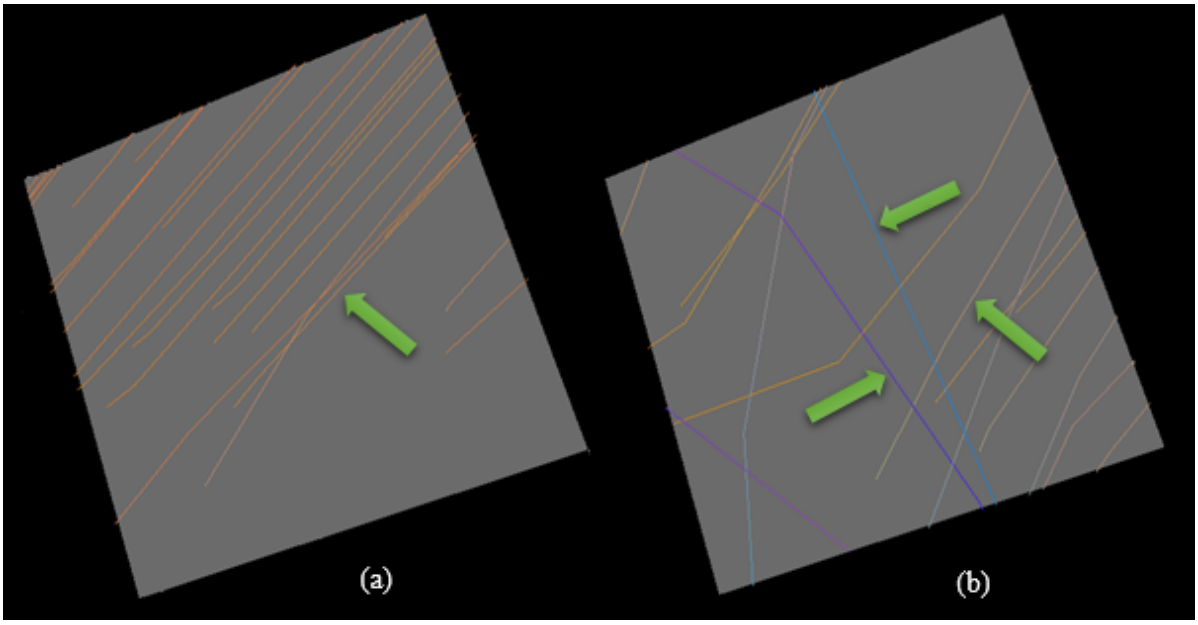

Figure 3.12: Isolated voxel depicting the streamlines passing through it. (a) DTI-based tractography detects only one orientation. Whereas (b) CSD-based tractography detects multiple orientations in the same voxel. Different directions are encoded in different colors (arrows).

Discussion:

As mentioned in the previous chapter, one of the limits of DTI is its poor estimation of multiple orientations within the same voxel. This method can only detect up to one orientation per voxel. Voxels with multiple fiber populations are either considered as isotropic voxels or the direction of the principle eigenvector is the only estimated orientation. Among others, CSD method have been developed in order to overcome this limitation. Figure 3.12 clearly depicts this difference. Several orientations were estimated within the same voxel using CSD-based tractography, unlike DTI-based tractography, where only the dominant direction was taken into consideration.

The complex connectivity exhibited by WM tracts cannot be illustrated using DTI-based tractography, which only shows the general connections between the major tracts.

3.5.3 Effect of reconstruction methods on the total number of generated streamlines

We applied both DTI- and CSD-based tractography on all three cases. Then, we tabulated the total number of streamlines generated using each method as follows:

	Total Number of Streamlines	
Reconstruction Method	**CSD**	**DTI**
Case 1	30516	24638
Case 2	45084	25765
Case 3	45523	28981

Table 3.3: Table displaying the total number of streamlines generated using CSD- and DTI-based tractography for all cases.

The following histogram illustrates the obtained results:

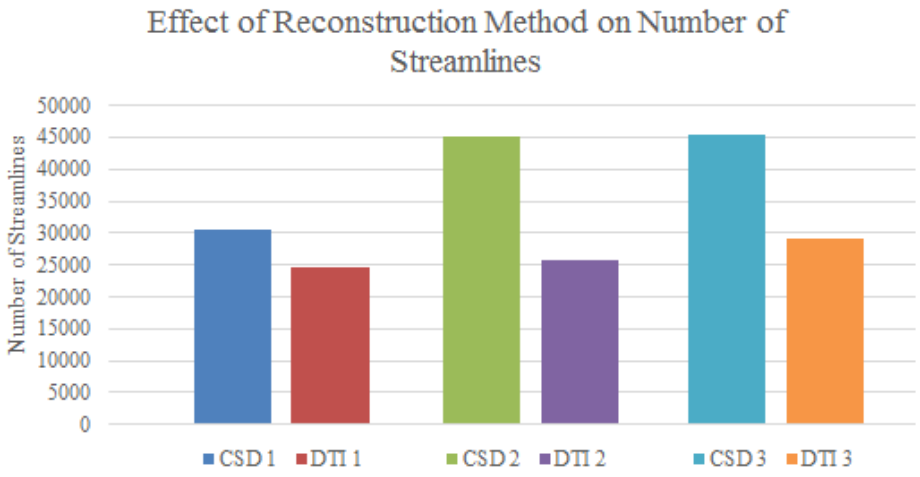

Figure 3.13: Histogram illustrating the difference between the number of generated streamlines using CSD- and DTI-based tractography for all cases.

Discussion:

From the histogram, we can see that the number of streamlines generated using CSD-based tractography is always larger than when using DTI-based tractography. The percentage of difference between the total number of streamlines generated using the two methods is: 21.3%, 54.5% and 44.4% in case1, case 2 and case 3, respectively.
The first case exhibited the least difference, this is mainly due to the considerable size of the tumor and its location which, as mentioned previously, cancels the construction of both the intralesional short fibers and fibers initiated from the tumoral region, thus reducing the

total number of the generated streamlines. Consequently, the regions of crossing fibers are significantly reduced, especially on the right hemisphere, which minimizes the difference between the performance of DTI-based tractography and the CSD-based one.
The second patient had the tumor in the corpus callosum, which is the tract connecting the left and right hemispheres. CC is characterized by its high FA value i.e. the fibers are mostly oriented in the same direction, hence damage to this region will decrease the anisotropy of the region. This also means that almost all of the regions comprising complex fiber populations are still intact. As such, DTI-based tractography lost one of its best reigons where anisotropy is highest, making the number of fibers generated using CSD-based tractography more than twice the number of streamlines generated using DTI-based tractography (54.5).
The last patient had a small tumor located in Wernicke's area. Compared to the previous case, the difference of 44.4% means that the tumoral region included some regions of crossing fibers, but it did not amount to much due to the small size of the tumor. Thus, the number of streamlines generated by CSD-based tractography is still very high compared to DTI-based tractography.

CSD-based tractography extracts more information from diffusion MRI data about the underlying microstructure of WM than DTI-based tractography does. However, this information comes with a constraint. The time needed to both acquire the necessary diffusion-weighted images and to perform all the analysis steps is too long to be clinically accepted. Applying CSD-based tractography in the daily clinical routine would be rather inefficient since the time usually spent to examine multiple patients would be barely enough for only one of them. DTI-based tractography is preferable to use in this case where the confirmation of the presence of the tumor and the overall tumor-induced alterations are possible to obtain in a clinically accepted time. Whereas, for the planning of a surgery, it is strongly recommended to use the results of CSD-based tractography since it offers more details on the tumor-induced alterations.

3.6 Assessment of the tumor-induced damage

3.6.1 Visual evaluation of the tumor

Using MI-Brain tool, we created a sequence of images, each representing an axial slice of a tractogram resulting from a CSD-based tractography. The consecutive images were constructed by increasing the length of the streamlines starting from 5mm until the maximum length. This was done for all three cases discussed previously.

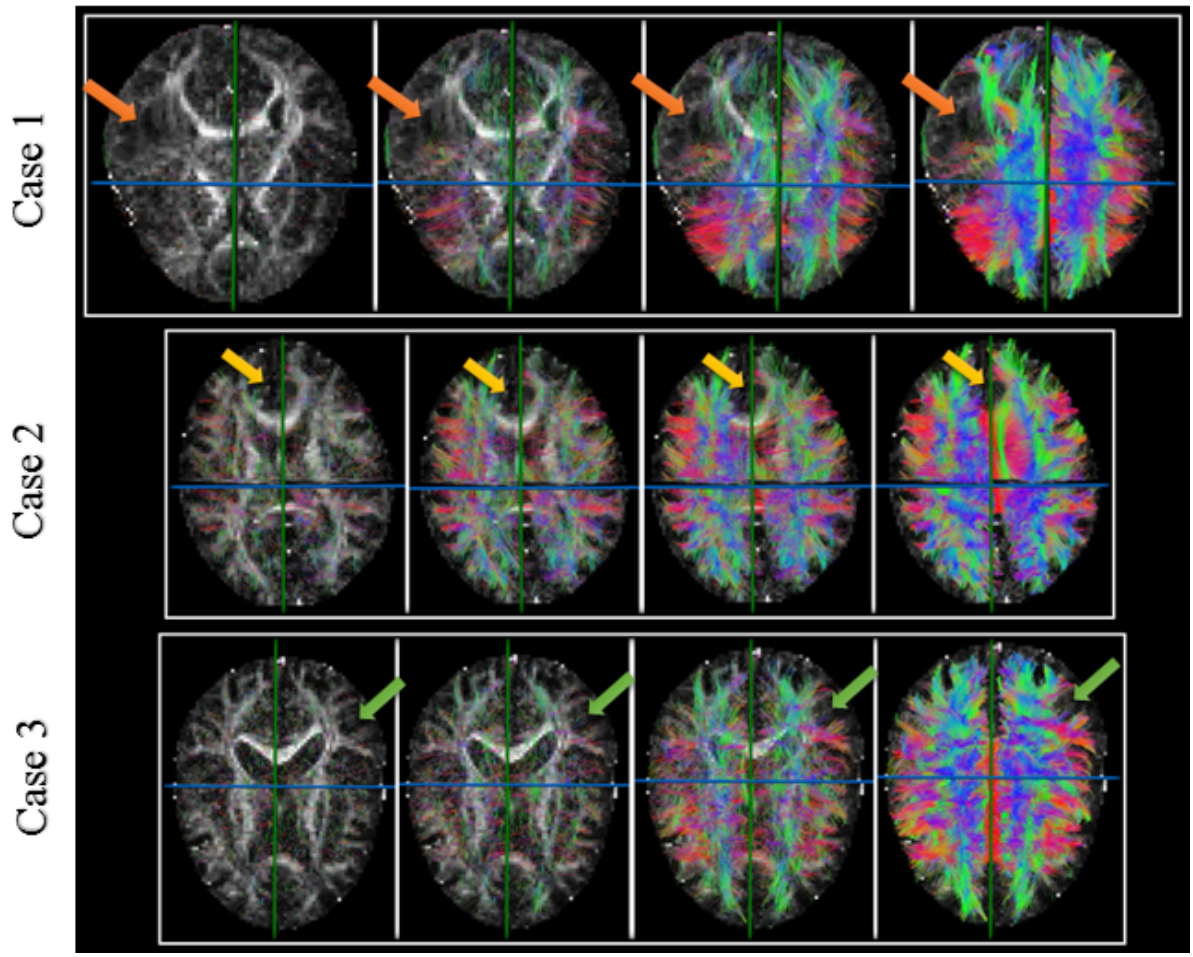

Figure 3.14: The illustration of the tractograms resulting from increasing the length of the streamlines. In all cases, the arrow shows the location of the tumor.

Discussion:

In these figures we observe that, in all cases, increasing the length of the streamlines does not affect the tumoral region. We notice that the streamlines always stop at the edge of the tumor, which can be attributed to either the destruction of the penetrating streamlines or their displacement, as seen in the previous study. This behavior is not noticeable on the adjacent hemisphere where the development of the streamlines seems natural and comparable to the behavior observed on a normal brain. This implies the fact that the presence of a tumor disturbs the normal behavior of the brain. We can further deduce that defective WM tissues decrease the intralesional anisotropy since the pathways, which define the directionality, are disconnected. It should be pointed out that these results are not always true for all tumors. The behavior of other types of lesions may vary due to unique characteristics exhibited by other pathologies.

3.6.2 Quantitative comparison between left and right brain hemispheres

In this section, we used MI-Brain tool's segmentation functions in order to separate the hemispheres of each patient. We then computed the following parameters: Number, mean length (mm) and the standard deviation (SD) (mm) of the streamlines in left and right hemispheres as well as the ones shared between the two (intersection). We then tabulated the results as follows:

	Case 1			Case 2			Case 3		
Hemisphere	**Number**	**Mean**	**SD**	**Number**	**Mean**	**SD**	**Number**	**Mean**	**SD**
Left	12722	30,1	21,1	19140	21,9	21,9	19350	25	23,8
Right	10475	30,3	24,9	18688	23,4	23,6	20214	23,9	24,1
Intersection	7319	46,5	21,3	7256	46,7	19,2	5959	50,4	24,9

Table 3.4: Table displaying the different parameters corresponding to left and right hemispheres and their intersection for the clinical cases. The results found on the hemisphere comprising the tumor are highlighted.

The same analysis was conducted on two datasets of normal brains provided by dipy's official website as example datasets:

	Normal Case 1			Normal Case 2		
Hemisphere	**Number**	**Mean**	**SD**	**Number**	**Mean**	**SD**
Left	45022	25,3	22,1	30702	67,3	47,4
Right	45639	24,2	22,4	30960	64,2	45
Intersection	6493	44,1	31,1	20264	116,8	44,2

Table 3.5: Table displaying the different parameters corresponding to left and right hemispheres and their intersection for the normal cases.

The following histograms were plotted after the normalization of the obtained values. We plotted only the left and right results which fall in the scope of this section:

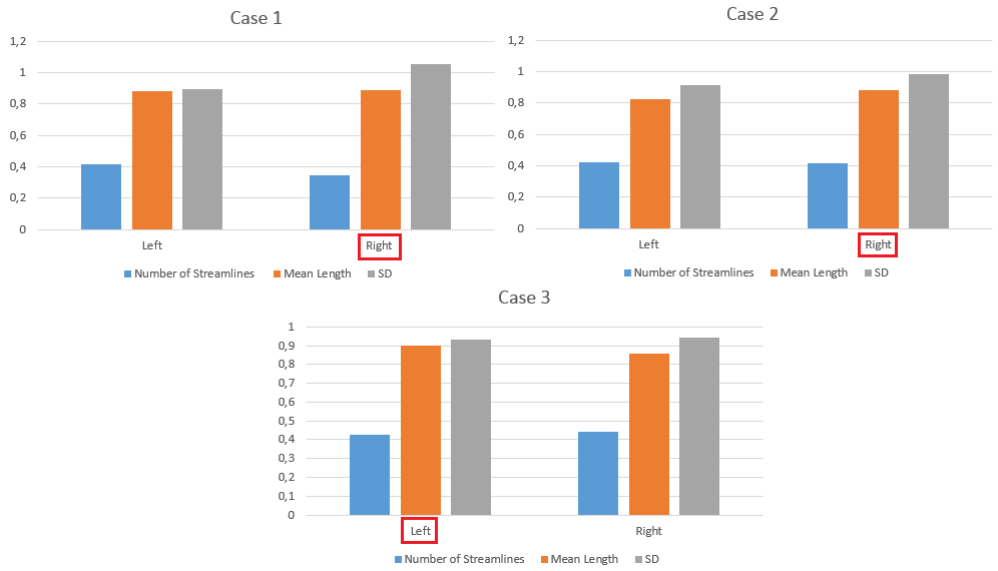

Figure 3.15: Histograms demonstrating the values of the parameters number, mean length and SD of left and right hemispheres for the clinical cases. The red box identifies the hemisphere containing the tumor.

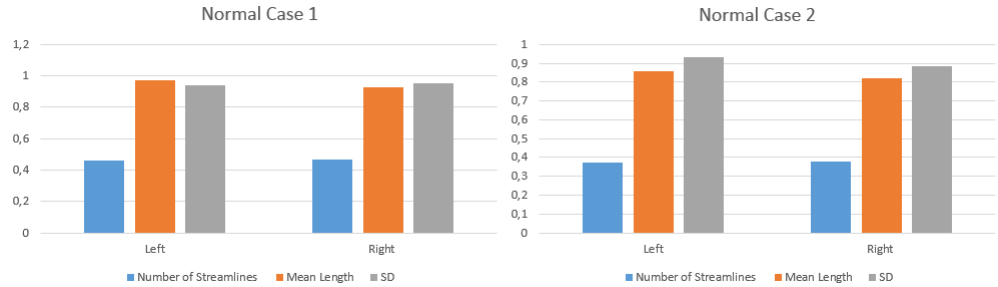

Figure 3.16: Histograms demonstrating the values of the parameters number, mean length and SD of left and right hemispheres for the normal cases.

Discussion:

In all clinical cases, the number of streamlines is smaller in the hemisphere where the tumor resides than in the adjacent hemisphere. The first patient demonstrated the highest difference between left and right (19,37%). The two other cases, however, did not exhibit much of a difference (2,38% and 4,36%) respectively. The two normal cases showed an arguably negligible difference of 1,36% and 0,83% for normal case 1 and normal case 2 respectively.

As seen in the previous study, streamlines were not able to penetrate the tumoral region, and none were initiated from it. This means that short fibers that only exist within the tumor are not constructed, thus reducing the number of streamlines in the hemisphere containing the tumor. This mostly depends on the size and location of the tumor. So the

high difference observed in the first case is mainly due to the massive size of the tumor. The second case had a tumor located in the right supplementary motor area, which falls in the intersection group, and therefore, the effect the tumor had on the calculated parameters was mostly not taken into account which explains the slight difference.
The last clinical case, likewise, exhibited a small difference but unlike the aforementioned case, the result here is due to different reasons. The patient had astrocytoma grade II, it was detected in Wernicke's area which is located in the superior part of the posterior temporal lobe in the dominant cerebral hemisphere, the left one for our patient. The tumor had a small size, so the number of intralesional fibers not reconstructed would be small. Moreover, as was indicated in the previous section, the streamlines were mainly displaced from their original pathway, hence no major reduction in numbers.
The normal cases showed the least difference in numbers of streamlines between left and right. This could be attributed to the absence of a tumor or any defective WM tissues. Given such results, it is possible to set a threshold of approximately 2% difference, where any percentage above could be an indicating factor of the presence of a tumor.

In the clinical cases, the mean length and standard deviation were slightly larger in the hemisphere containing the tumor compared to the adjacent one, except for the last case where the SD is smaller in the hemisphere comprising the tumor. In both the normal and the clinical cases, the differences in mean length were mostly trivial and amounted to 0.2mm, 1.7mm and 1.1mm in clinical cases 1, 2 and 3 respectively; and to 0.3mm and 2.4mm in normal cases 1 and 2 respectively. All cases displayed high standard deviation values, all exceeding 20mm (exceeding 40mm in normal case 2). This implies that the length of the streamlines generated has a wide range of variation.

In both normal and clinical cases, the number of streamlines shared between the hemispheres is significantly smaller compared to the number of streamlines found on each side. This is expected since only the commissural fibers connecting the two hemispheres are counted. Compared to the results shown above, the intersection group is characterized with a larger mean length and a similar standard deviation.

From these findings, we deduce that, aside from mean length and standard deviation of the streamlines which proved to be unreliable parameters, we can set the difference in number of streamlines between left and right hemispheres as an alerting factor where an elevated percentage may suggest the presence of a tumor and may call for further investigation.

It should be mentioned that these results are prone to several errors. First, acquisition, reconstruction and tractography errors discussed in the previous chapters which affect the quality of the streamlines generated. Second, the hemispheres were segmented manually which may lead to incorrect values. Lastly, the number of clinical and normal cases studied

is minimal and therefore did not cover all the possible behaviors.

It is to note that all the obtained results were verified, commented and validated by a group of radiologists from the Hospital of CHAHIDS MAHMOUDI - Tizi Ouzou, and researchers from INRIA in the Sophia Antipolis-Méditérannée Research Center and Sherbrooke Connectivity Imaging Lab (SCIL), University of Sherbrooke-Canada.

3.7 Summary

Tumors affect WM tracts in different ways. The size, the location and the grade of the tumor are some of the major factors that determine the nature of the WM tracts alteration. Three kinds of these alterations were disclosed in this experiment: destruction, displacement, or destruction with displacement of the streamlines located within and around the tumor. It was also shown that all cases displayed a decrease in the intralesional FA value. These findings are meant to serve as side guidelines for neurosurgeons while preparing the surgical strategy.

A comparison between DTI- and CSD-based tractography methods revealed the following results:

- Both methods were able to confirm the presence of the tumor in addition to the affected major WM tracts.
- CSD-based tractography offers more information about the underlying WM microstructure, while DTI-based tractography only performs well in regions of high anisotropy.
- It is more effective to use DTI-based tractography in the daily clinical routine, and CSD-based tractography in highly sensitive tasks such as the planning of a surgery.

A quantitative comparison between the left and right hemispheres was conducted on both clinical and normal cases, in order to determine some factors that may help in exposing the existence of a tumor. After evaluating the difference between the two using various parameters, namely: the number, the mean length and the standard deviation of the streamlines, we concluded that the number of streamlines generated may alert to the presence of a tumor, that is by detecting a high difference in number of streamlines between left and right hemispheres (or by exceeding a threshold of 2% difference). Both the mean length and the standard deviation proved to be unreliable parameters to use in the detection of a tumor.

General Conclusion

In conclusion, we have disclosed in this work the different effects astrocytomas have on WM tracts. This was accomplished thanks to diffusion MRI technique that allows the reconstruction of the axonal microstructure of the brain. The background knowledge on dMRI and its physical basis was given in the first chapter. In the second chapter, we tackled the different aspects of this field, starting by introducing reconstruction methods, namely : DTI and HARDI-based techniques Q-ball and CSD ; then concluding the theoretical part by shedding some light on tractography, currently the only technique that can reconstruct and visualize WM bundles in 3D. We presented the two major classes of tractography, the deterministic and the probabilistic.

Given our objective, we started by collecting the data that met our needs. The UK Data Archive provided the necessary datasets which were used in our study. We chose three patients presented with different grades of astrocytomas to observe their behaviors. This was achieved by applying diffusion analysis on their respective data. Recall that such analysis involves several essential steps : the acquisition of data, the preprocessing which consists of converting the data and removing the background, the processing which entails the estimation of the local orientations and the 3D reconstruction of the fibers using deterministic tractography, and finally the visualization of the tractograms in order to assess the damage and identify the tumor-induced alterations.

The alteration of WM tracts by astrocytoma produced three distinct patterns : the destruction and displacement of WM tracts observed in the patient with the grade IV astrocytoma. The destruction of the intralesional fibers which was detected in the patient with grade III astrocytoma. And finally the displacement of the surrounding tracts that was revealed in the patient with the grade II astrocytoma. All analyzed cases exhibited a decrease in the intralesional FA value. The purpose of such a study is to assist neurosurgeons in their work. Observing the nature of the alteration caused by the tumor before performing a surgery may help in deciding the course of action that would allow the surgeon to preserve the functionality of the brain while excising the tumor.

Given that the previous study was conducted using the CSD-based tractography, we decided to investigate the results of the same analysis but using DTI-based tractogrpahy in

order to assess the difference between the two methods. We concluded that both methods confirmed the presence of the tumor and identified the resulting alterations. Following these findings, we further explored the difference between the two methods by means of a quantitative comparison. We used the number of generated streamlines as a comparative parameter. It was revealed that a considerable amount of information was lost using DTI-based tractography. This was attributed to the fact that DTI detects only one orientation per voxel while ignoring the other directions in case of multiple fiber populations. This led to the conclusion that DTI-based tractography is better suited to the daily clinical routine where the confirmation of the existence of the tumor and its induced alterations are possible in a clinically acceptable time. Whereas, CSD-based tractography is used in preoperative procedures, among other tasks that do not take into consideration the long acquisition time.

Finally, we assessed the tumor-induced damage by : on one hand, visually observing the tumoral region while increasing the length of the streamlines, this showed the tumoral region void of any penetrating streamlines thus further confirming our earlier discoveries of either the destruction and/or the displacement of the fibers surrounding the tumor. On the other hand, quantitatively comparing the left and right brain hemispheres of both normal and clinical cases. This was done in the hope of finding some parameter that would help in determining the existence of a tumor. Three such parameters were evaluated : the number, the mean length and the standard deviation of the streamlines residing in either left or right hemispheres, or in the intersection region connecting the two. Both the mean length and the standard deviation of the streamlines were proved as unreliable factors. The number of streamlines, however, was set as an indicator to the existence of the tumor.

Overall, this project allowed us to dive into the vast field of diffusion MRI and its wide range of application. It is a relatively recent technique that holds a very promising future. Moreover, with the variety of brain pathologies that affect both children and adults, this work can be further exploited to :

- Investigate the effects of other kinds of diseases.
- Identify new disease biomarkers, thus allowing the early treatment of the affected region.
- Adapt the analysis to new developed techniques in order to achieve better results.

Finally, we hope that this modest work contributes, however slight it may be, to the improvement of the neurosurgical filed and help students better understand this vast area of knowledge.

Bibliography

Anderson, Adam W. 2001. Theoretical analysis of the effects of noise on diffusion tensor imaging. *Magnetic Resonance in Medicine*, **46**(6), 1174–1188.

Basser, Peter J, & Pierpaoli, Carlo. 1998. A simplified method to measure the diffusion tensor from seven MR images. *Magnetic resonance in medicine*, **39**(6), 928–934.

Basser, Peter J, Mattiello, James, & LeBihan, Denis. 1994a. Estimation of the effective self-diffusion tensor from the NMR spin echo. *Journal of Magnetic Resonance, Series B*, **103**(3), 247–254.

Basser, Peter J, Mattiello, James, & LeBihan, Denis. 1994b. MR diffusion tensor spectroscopy and imaging. *Biophysical journal*, **66**(1), 259–267.

Basser, Peter J, Pajevic, Sinisa, Pierpaoli, Carlo, Duda, Jeffrey, & Aldroubi, Akram. 2000. In vivo fiber tractography using DT-MRI data. *Magnetic resonance in medicine*, **44**(4), 625–632.

Beaulieu, Christian. 2002. The basis of anisotropic water diffusion in the nervous system–a technical review. *NMR in Biomedicine*, **15**(7-8), 435–455.

Behrens, Timothy EJ, Berg, H Johansen, Jbabdi, Saad, Rushworth, Matthew FS, & Woolrich, Mark W. 2007. Probabilistic diffusion tractography with multiple fibre orientations: What can we gain? *Neuroimage*, **34**(1), 144–155.

Brown, Robert. 1828. XXVII. A brief account of microscopical observations made in the months of June, July and August 1827, on the particles contained in the pollen of plants; and on the general existence of active molecules in organic and inorganic bodies. *The Philosophical Magazine*, **4**(21), 161–173.

Cherifi, Dalila, Chellouche, Ali, Ouakli, Amazigh Ait, Benamara, Youcef, & Deriche, Rachid. 2013. Tensor estimation and visualization using dMRI. *Pages 61–68 of: Systems, Signal Processing and their Applications (WoSSPA), 2013 8th International Workshop on*. IEEE.

Cherifi, Dalila, Boudjada, Messaoud, Morsli, Abdelatif, Girard, Gabriel, & Deriche, Rachid. 2018. Combining Improved Euler and Runge-Kutta 4th order for Tractography in Diffusion-Weighted MRI. *Biomedical Signal Processing and Control*, **41**, 90–99.

Clarisse, Perrine. 2008. *Tractographie cérébrale par IRM de tenseur de diffusion: influence des paramètres d'acquisition et de la méthode de tractographie sur la reproductibilité et la plausibilité anatomique des résultats dans la perspective d'une application en routine clinique*. Ph.D. thesis, Université de Toulouse, Université Toulouse III-Paul Sabatier.

Conturo, Thomas E, Lori, Nicolas F, Cull, Thomas S, Akbudak, Erbil, Snyder, Abraham Z, Shimony, Joshua S, McKinstry, Robert C, Burton, Harold, & Raichle, Marcus E. 1999. Tracking neuronal fiber pathways in the living human brain. *Proceedings of the National Academy of Sciences*, **96**(18), 10422–10427.

Côté, Marc-Alexandre, Girard, Gabriel, Boré, Arnaud, Garyfallidis, Eleftherios, Houde, Jean-Christophe, & Descoteaux, Maxime. 2013. Tractometer: towards validation of tractography pipelines. *Medical image analysis*, **17**(7), 844–857.

Demi, L, Verweij, MD, & Brahme, A. 2014. Nonlinear acoustics. *Comprehensive Biomedical Physics*, 387–399.

Descoteaux, Maxime. 2008. *High angular resolution diffusion MRI: from local estimation to segmentation and tractography*. Ph.D. thesis, Université Nice Sophia Antipolis.

Descoteaux, Maxime. 2015. High angular resolution diffusion imaging (hardi). *Wiley Encyclopedia of Electrical and Electronics Engineering*.

Descoteaux, Maxime, & Poupon, Cyril. 2012. Diffusion-weighted MRI. *Comprehensive Biomedical Physics*, **3**(6), 81–97.

Descoteaux, Maxime, Angelino, Elaine, Fitzgibbons, Shaun, & Deriche, Rachid. 2007. Regularized, fast, and robust analytical Q-ball imaging. *Magnetic resonance in medicine*, **58**(3), 497–510.

Descoteaux, Maxime, Deriche, Rachid, Knosche, Thomas R, & Anwander, Alfred. 2009. Deterministic and probabilistic tractography based on complex fibre orientation distributions. *IEEE transactions on medical imaging*, **28**(2), 269–286.

Einstein, Albert. 1956. *Investigations on the Theory of the Brownian Movement*. Courier Corporation.

Essayed, Walid I, Zhang, Fan, Unadkat, Prashin, Cosgrove, G Rees, Golby, Alexandra J, & O'Donnell, Lauren J. 2017. White matter tractography for neurosurgical planning:

A topography-based review of the current state of the art. *NeuroImage: Clinical*, **15**, 659–672.

Fick, Adolph. 1995. On liquid diffusion. *Journal of Membrane Science*, **100**(1), 33–38.

Hess, Christopher P, Mukherjee, Pratik, Han, Eric T, Xu, Duan, & Vigneron, Daniel B. 2006. Q-ball reconstruction of multimodal fiber orientations using the spherical harmonic basis. *Magnetic Resonance in Medicine*, **56**(1), 104–117.

Jeurissen, B, Leemans, A, Tournier, JD, Jones, DK, & Sijbers, J. 2010. Estimating the number of fiber orientations in diffusion MRI voxels: a constrained spherical deconvolution study. *Page 573 of: International Society for Magnetic Resonance in Medicine (ISMRM)*.

Jeurissen, Ben. 2012. *Improved analysis of brain connectivity using high angular resolution diffusion MRI*. Ph.D. thesis, Universiteit Antwerpen (Belgium).

Jeurissen, Ben, Leemans, Alexander, Tournier, Jacques-Donald, & Sijbers, Jan. 2009. Fiber tracking on the 'fiber cup phantom'using constrained spherical deconvolution. *Pages 232–235 of: Medical Image Computing and Computer-Assisted Intervention (MICCAI) Workshop on Diffusion Modelling and the Fiber Cup (DMFC'09)*.

Jeurissen, Ben, Leemans, Alexander, Jones, Derek K, Tournier, Jacques-Donald, & Sijbers, Jan. 2011. Probabilistic fiber tracking using the residual bootstrap with constrained spherical deconvolution. *Human brain mapping*, **32**(3), 461–479.

Johansen-Berg, Heidi, & Behrens, Timothy EJ. 2013. *Diffusion MRI: from quantitative measurement to in vivo neuroanatomy*. Academic Press.

Jones, Derek K. 2003. Determining and visualizing uncertainty in estimates of fiber orientation from diffusion tensor MRI. *Magnetic Resonance in Medicine*, **49**(1), 7–12.

Jones, Derek K. 2004. The effect of gradient sampling schemes on measures derived from diffusion tensor MRI: a Monte Carlo study. *Magnetic Resonance in Medicine*, **51**(4), 807–815.

Lazar, Mariana, & Alexander, Andrew L. 2003. An error analysis of white matter tractography methods: synthetic diffusion tensor field simulations. *Neuroimage*, **20**(2), 1140–1153.

Lazar, Mariana, Weinstein, David M, Tsuruda, Jay S, Hasan, Khader M, Arfanakis, Konstantinos, Meyerand, M Elizabeth, Badie, Benham, Rowley, Howard A, Haughton, Victor, Field, Aaron, *et al.* 2003. White matter tractography using diffusion tensor deflection. *Human brain mapping*, **18**(4), 306–321.

Le Bihan, Denis. 2003. Looking into the functional architecture of the brain with diffusion MRI. *Nature Reviews Neuroscience*, **4**(6), 469.

Le Bihan, Denis, Breton, Eric, Lallemand, Denis, Grenier, Philippe, Cabanis, Emmanuel, & Laval-Jeantet, Maurice. 1986. MR imaging of intravoxel incoherent motions: application to diffusion and perfusion in neurologic disorders. *Radiology*, **161**(2), 401–407.

Le Bihan, Denis, Turner, Robert, Moonen, Chrit TW, & Pekar, James. 1991. Imaging of diffusion and microcirculation with gradient sensitization: design, strategy, and significance. *Journal of Magnetic Resonance Imaging*, **1**(1), 7–28.

Leemans, A, Sijbers, J, Verhoye, M, Van der Linden, A, & Van Dyck, D. 2005. Mathematical framework for simulating diffusion tensor MR neural fiber bundles. *Magnetic resonance in medicine*, **53**(4), 944–953.

Lin, Ching-Po, Tseng, Wen-Yih Isaac, Cheng, Hui-Cheng, & Chen, Jyh-Horng. 2001. Validation of diffusion tensor magnetic resonance axonal fiber imaging with registered manganese-enhanced optic tracts. *Neuroimage*, **14**(5), 1035–1047.

Lori, NF, Akbudak, E, Shimony, JS, Cull, TS, Snyder, AZ, Guillory, RK, & Conturo, TE. 2002. Diffusion tensor fiber tracking of human brain connectivity: aquisition methods, reliability analysis and biological results. *NMR in Biomedicine*, **15**(7-8), 494–515.

Mori, Susumu, Crain, Barbara J, Chacko, Vadappuram P, & Van Zijl, Peter CM. 1999. Three-dimensional tracking of axonal projections in the brain by magnetic resonance imaging. *Annals of Neurology: Official Journal of the American Neurological Association and the Child Neurology Society*, **45**(2), 265–269.

Mukherjee, P, Berman, JI, Chung, SW, Hess, CP, & Henry, RG. 2008. Diffusion tensor MR imaging and fiber tractography: theoretic underpinnings. *American journal of neuroradiology*, **29**(4), 632–641.

Nimsky, Christopher, Ganslandt, Oliver, & Fahlbusch, Rudolf. 2006. Implementation of fiber tract navigation. *Operative Neurosurgery*, **58**(suppl_4), ONS–292.

Paragios, Nikos, Duncan, James, & Ayache, Nicholas. 2010. *Handbook of Biomedical Imaging*. Springer.

Parker, Geoffrey JM, & Alexander, Daniel C. 2005. Probabilistic anatomical connectivity derived from the microscopic persistent angular structure of cerebral tissue. *Philosophical Transactions of the Royal Society B: Biological Sciences*, **360**(1457), 893–902.

Pernet, Cyril R, Gorgolewski, Krzysztof J, Job, Dominic, Rodriguez, David, Whittle, Ian, & Wardlaw, Joanna. 2016. A structural and functional magnetic resonance imaging dataset of brain tumour patients. *Scientific data*, **3**, 160003.

Perrin, Muriel, Poupon, Cyril, Rieul, Bernard, Leroux, Patrick, Constantinesco, André, Mangin, Jean-François, & LeBihan, Denis. 2005. Validation of q-ball imaging with a diffusion fibre-crossing phantom on a clinical scanner. *Philosophical Transactions of the Royal Society B: Biological Sciences*, **360**(1457), 881–891.

Pierpaoli, Carlo, Jezzard, Peter, Basser, Peter J, Barnett, Alan, & Di Chiro, Giovanni. 1996. Diffusion tensor MR imaging of the human brain. *Radiology*, **201**(3), 637–648.

Pullens, Pim, Roebroeck, Alard, & Goebel, Rainer. 2010. Ground truth hardware phantoms for validation of diffusion-weighted MRI applications. *Journal of Magnetic Resonance Imaging*, **32**(2), 482–488.

Raichle, Marcus E, MacLeod, Ann Mary, Snyder, Abraham Z, Powers, William J, Gusnard, Debra A, & Shulman, Gordon L. 2001. A default mode of brain function. *Proceedings of the National Academy of Sciences*, **98**(2), 676–682.

Savadjiev, Peter, Campbell, Jennifer SW, Descoteaux, Maxime, Deriche, Rachid, Pike, G Bruce, & Siddiqi, Kaleem. 2008. Labeling of ambiguous subvoxel fibre bundle configurations in high angular resolution diffusion MRI. *NeuroImage*, **41**(1), 58–68.

Soares, Jose, Marques, Paulo, Alves, Victor, & Sousa, Nuno. 2013. A hitchhiker's guide to diffusion tensor imaging. *Frontiers in neuroscience*, **7**, 31.

Stejskal, Edward O, & Tanner, John E. 1965. Spin diffusion measurements: spin echoes in the presence of a time-dependent field gradient. *The journal of chemical physics*, **42**(1), 288–292.

Tensaouti, Fatima. 2010. *Tractographie par IRM de diffusion: algorithmes, validation, reproductibilité et applications*. Ph.D. thesis, Université de Toulouse, Université Toulouse III-Paul Sabatier.

Tournier, J-Donald, Calamante, Fernando, Gadian, David G, & Connelly, Alan. 2004. Direct estimation of the fiber orientation density function from diffusion-weighted MRI data using spherical deconvolution. *NeuroImage*, **23**(3), 1176–1185.

Tournier, J-Donald, Calamante, Fernando, & Connelly, Alan. 2007. Robust determination of the fibre orientation distribution in diffusion MRI: non-negativity constrained super-resolved spherical deconvolution. *Neuroimage*, **35**(4), 1459–1472.

Tuch, David S. 2004. Q-ball imaging. *Magnetic resonance in medicine*, **52**(6), 1358–1372.

Tuch, David Solomon, *et al.* 2002. *Diffusion MRI of complex tissue structure*. Ph.D. thesis, Massachusetts Institute of Technology.

Vincent, Justin L, Patel, Gaurav H, Fox, Michael D, Snyder, Abraham Z, Baker, Justin T, Van Essen, David C, Zempel, John M, Snyder, Lawrence H, Corbetta, Maurizio, & Raichle, Marcus E. 2007. Intrinsic functional architecture in the anaesthetized monkey brain. *Nature*, **447**(7140), 83.

Wedeen, Van J, Wang, RP, Schmahmann, Jeremy D, Benner, Thomas, Tseng, WYI, Dai, Guangping, Pandya, DN, Hagmann, Patric, D'Arceuil, Helen, & de Crespigny, Alex J. 2008. Diffusion spectrum magnetic resonance imaging (DSI) tractography of crossing fibers. *Neuroimage*, **41**(4), 1267–1277.

Wedeen, VJ, Reese, TG, Tuch, DS, Weigel, MR, Dou, JG, Weiskoff, RM, & Chessler, D. 2000. Mapping fiber orientation spectra in cerebral white matter with Fourier-transform diffusion MRI. *Page 82 of: Proceedings of the 8th Annual Meeting of ISMRM, Denver*.

Westin, C-F, Maier, Stephan E, Mamata, Hatsuho, Nabavi, Arya, Jolesz, Ferenc A, & Kikinis, Ron. 2002. Processing and visualization for diffusion tensor MRI. *Medical image analysis*, **6**(2), 93–108.